

Article

Research on Internal Flow Field Characteristics of Straight-Groove Texture Using Three-Dimensional Modeling

Yulong Li, Zhehao Zhang, Yongyong He * and Jianbin Luo

State Key Laboratory of Tribology in Advanced Equipment, Tsinghua University, Beijing 100084, China

* Correspondence: hey@mail.tsinghua.edu.cn; Tel./Fax: +86-10-62787932

Abstract: Surface texture modification is a reasonable strategy for improving the tribological property of friction pairs. The internal flow behavior of the surface texture significantly impacts its performance. In this study, a three-dimensional computational fluid dynamics (CFD) model is constructed to explore the internal flow behavior of the straight-groove texture in the thrust bearing. The influences of the Reynolds number, depth ratio, and area ratio of the straight-groove texture on the internal flow behavior are systematically investigated. Furthermore, the streamline and tribological performance parameters are checked to reveal the mechanism of the groove texture influencing the tribological properties. It is found that the vortex and cavitation significantly affect the tribological performance of textured surfaces under hydrodynamic lubrication. The cavitation and upstream vortex areas increase with the Reynolds number, while the downstream vortex area shows a reverse trend. The increase in depth ratio strengthens the upstream and downstream vortices while reducing the cavitation area. Additionally, a method is proposed to determine the location of the cavitation within the groove texture. Certain operating conditions create the optimal texture depth ratio and area ratio, which could maximize the load-carrying capacity (LCC) of the oil film, and the friction coefficient is relatively small.

Keywords: surface texture; LCC; CFD; vortex; cavitation; mechanism



Citation: Li, Y.; Zhang, Z.; He, Y.; Luo, J. Research on Internal Flow Field Characteristics of Straight-Groove Texture Using Three-Dimensional Modeling. *Lubricants* **2023**, *11*, 338. <https://doi.org/10.3390/lubricants11080338>

Received: 9 July 2023

Revised: 30 July 2023

Accepted: 4 August 2023

Published: 9 August 2023



Copyright: © 2023 by the authors. Licensee MDPI, Basel, Switzerland. This article is an open access article distributed under the terms and conditions of the Creative Commons Attribution (CC BY) license (<https://creativecommons.org/licenses/by/4.0/>).

1. Introduction

In 1966, Hamilton [1] presented that small irregularities on flat, parallel friction surfaces could generate asymmetric pressure distribution. The integrated effect of small irregularities and associated film cavities is the primary regime for load-carrying capacity (LCC) between friction pairs. The small irregularities on the interfacial surfaces are later called surface texture. In 1996, Etsion [2] explored the sealing properties of non-contacting mechanical seals with hemispherical pores using numerical calculation. It is found that there is an optimum dimple parameter to obtain the largest LCC and minimum friction torque. This optimal pore size depended on the viscosity, the sealing pressure, and the area ratio of pores. Due to the significant advantages in improving tribological performance in the LCC, wear resistance, and friction reduction, surface texture has attracted more and more attention from scholars. In addition, with significant advancements in modern manufacturing industries, surface texture is now extensively employed to boost lubrication properties in various industrial components such as mechanical face seals [3,4], piston ring–cylinder liner components [5,6], hydraulic pumps [7,8], gears [9], and thrust bearings [10,11].

The mechanism of texture on tribological properties varies under various lubricated regimes. The surface texture can generate a supplemental hydrodynamic effect during full-film or mixed lubrication, which is beneficial for increasing the LCC. Under a starved oil lubrication condition, the surface texture acts as the reservoir of the lubricant and serves as a secondary lubrication provision to the friction pairs. In addition, the surface texture can keep wear debris and prevent seizure under boundary or mixed lubrication. Some

other theories have also been proposed to explain the positive influence of surface texture. Local cavitation is the earliest theory used to demonstrate the load support mechanism [1], and the inertial effect [12–14], entrainment, and inlet suction [15,16] are also believed to be the reason for the enhancement of LCC.

Previous researchers developed numerical models of surface texture and solved the Reynolds or Navier–Stokes equation to predict various tribological properties, including pressure, film thickness, and frictional force [17]. These two major governing equations are widely used due to the excellent agreement between numerical models and experimental results. However, some scholars indicated that the Reynolds formula is inaccurate, and the Navier–Stokes formula is required under the following conditions: (1) high depth-to-diameter ratio in the surface texture [18]; (2) inertia effects are considered [19]; (3) the Reynolds number is larger than 8 [20]; (4) the texture depth is over ten percent of the oil thickness [21]. Because the Navier–Stokes equation is very complex, commercial CFD software is used for surface texture modeling.

Cavitation is a significant phenomenon in the surface texture, which has a critical influence on tribological properties, so the cavitation effect should be considered when conducting texture modeling. Hamilton [1] pointed out that the cavitation in the texture can suppress the very low pressure, and the cavitating pressure keeps invariable, which makes the high pressures overbalance the low pressures in the surface textures, leading to considerable LCC between friction pairs. Dowson [22] first observed the cavitation between a fixed perspex convex lens and a moving steel surface in 1957. The gas bubbles were split into a series of discrete bubbles by the streams of lubricating oil. Two main regimes of cavitation are accepted by researchers under fluid lubrication conditions. When the local pressure in the divergent region of surface texture drops below the gas-saturated vapor pressure, part of the lubricating oil undergoes a phase transition and converts to oil vapor. When the local pressure is smaller than the atmospheric pressure, the solubility of the air dissolved in the lubricating fluid is reduced accordingly, causing the air to escape from the lubricating fluid, and cavitation occurs. Zhang and Meng [23] performed the experimental observation and simulated prediction of cavitation region morphology in the straight-groove texture. The cavitation region morphology, cavitation area ratio, and frictional coefficient predicted by simulation were consistent with the experiment. Li et al. [24] also observed oil film rupture and formation if the local pressure dropped below atmospheric pressure. The saturated vapor pressure of lubricating oil is significantly lower than atmospheric pressure at ambient temperature and pressure. Thus, the second cavitation mechanism generally dominates in published papers.

Shi and Ni [25] established a two-dimensional CFD model with FLUENT. The influences of the sliding velocity, sliding pitch angle, texture scale, and cavitation pressure on friction performance are investigated. Xie et al. [26] also built a two-dimensional CFD model with cavitation to explore the interface lubrication regimes of microcavities in water-lubricated journal bearings. Their research showed that the microcavities could preserve lubricating fluid and create microhydrodynamic effects, and the accuracy of the theoretical model was confirmed by an experiment. Caramia et al. [27] performed CFD analysis for two-dimensional steady-state flow between two parallel textured surfaces. They analyzed the effect of surface texture settings on frictional force without considering cavitation. Their calculating and test results showed a considerable discrepancy in the reduction in the frictional force, which may be caused by neglecting cavitation effects. As analyzed in the above literature, cavitation may occur at the divergent wedge of the surface texture under full-film lubrication, influencing the lubrication properties of the friction pairs. Consequently, the influence of the cavitation effect should be considered when performing numerical analysis on friction pairs with surface texture. Moreover, CFD can be used to analyze the internal flow behavior of the texture so that the influences of texture settings on the tribological properties can be deeply explored.

In addition to cavitation, the vortex in the flow behavior of surface texture is another critical factor influencing tribological performance. Shen et al. [28] performed a

two-dimensional CFD numerical simulation of parallel sliding bearings under full-film lubrication. The stationary surface was textured with a chevron shape. The vortex first appeared at the bottom of the divergent wedge and extended with a decrease in texture length. They thought the vortex could consume kinetic energy and reduce the LCC. Wang et al. [29] analyzed the internal flow behavior of groove textures in the thrust bearing numerically, and their numerical calculation was also based on a two-dimensional CFD model. Their results showed that cavitation and vortex could exist simultaneously or that only one can form at the bottom of the texture, and both phenomena affected the hydrodynamic effect. Li et al. [30] established a three-dimensional CFD model of a dimpled friction pair to analyze the tribological performance for different Reynolds numbers, texture densities, and aspect ratios. They found that the primary regime for the texture to improve the lubrication property is the coupling effect of the wedge and the vortex. On the basis of the above references, the vortex may occur in specific surface texture parameters under hydrodynamic lubrication, affecting the internal flow behavior of surface texture. Therefore, the vortex can influence the lubrication property of the friction pair.

As found in the above research, the internal oil flow behavior of the texture is analyzed by employing a two-dimensional CFD model in many studies. Nevertheless, this widely used two-dimensional model has several disadvantages. Firstly, some studies simplified the rotational motion of the thrust bearing to periodic linear motion, neglecting the variations in circumferential velocity at different radial positions. Secondly, the two-dimensional model assumed the texture length was significantly larger than the width of the calculating domain and neglected the presence of side flow, thereby deviating from the actual working conditions. Furthermore, the two-dimensional CFD model could only reflect the flow behavior within a specific surface texture plane and failed to capture the precise flow behavior inside the texture fully. Consequently, the simplified two-dimensional model cannot be utilized to analyze the internal flow behavior of surface texture accurately and comprehensively. Moreover, the cavitation and vortex within the texture are investigated separately, and the interrelationship between these two phenomena remains unclear. The mechanism of surface texture improving lubricating performance has not been analyzed from the perspective of flow behavior.

Zhang and Meng [23] employed the straight-groove texture to analyze the influence of cavitation on the frictional properties experimentally and numerically. Shi and Ni [25] investigated the influence of straight-groove texture on the hydrodynamic pressure effect considering cavitation, and Wang et al. [29] also investigated the inner flow field of the straight-groove texture. In order to facilitate numerical model verification and show the advantages of the three-dimensional CFD model, the straight-groove texture is selected as the texture geometry.

This study constructs a three-dimensional CFD model to comprehensively analyze the internal flow behavior of straight-groove texture in the thrust bearing under hydrodynamic lubrication, which is validated by comparing the simulations with the test results in ref. [23]. The continuity equation and momentum equation are solved using the software FLUENT, considering the cavitation effect in the lubricating oil. The influences of the Reynolds number, depth ratio, and area ratio on the tribological performance are analyzed. Additionally, a prediction method for determining the cavitation position within the texture is presented. More importantly, the mechanism of groove texture on lubrication is explored from the perspective of flow behavior.

2. Method

2.1. Physical Model

Figure 1 presents the physical model of a ring–ring friction pair, which is the basic pairing form for a thrust bearing, valve plate, cylinder block in axial piston pump, etc. The upper surface is smooth and rotates at a constant speed n_r in the clockwise direction. The textured lower surface is stationary. Due to the coaxial rotary motion of the two rings, a cylindrical coordinate system is defined: r , θ , and z in Figure 1a represent the radial,

azimuth, and axial coordinates, respectively. The axis of rotation is at the position of $r = 0$, and the plane $z = 0$ is coplanar with the surface formed by the land area of the lower ring. The friction pair is fully immersed in lubricating oil. There are 24 straight grooves equally distributed in the circumferential direction on the lower ring, as presented in Figure 1b; the light blue zones are straight grooves; and the grey zones represent lands. Due to the periodicity, a fan-shaped sector in Figure 1c containing one straight groove is extracted for theoretical investigation. The circumferential angle of this sector is θ_0 , and the counterpart of the groove is θ_g . The inner and outer radii of the two rings are r_i and r_o , respectively. As shown in Figure 1d, the texture depth is d_g , and the oil thickness between the two rings is h_0 .

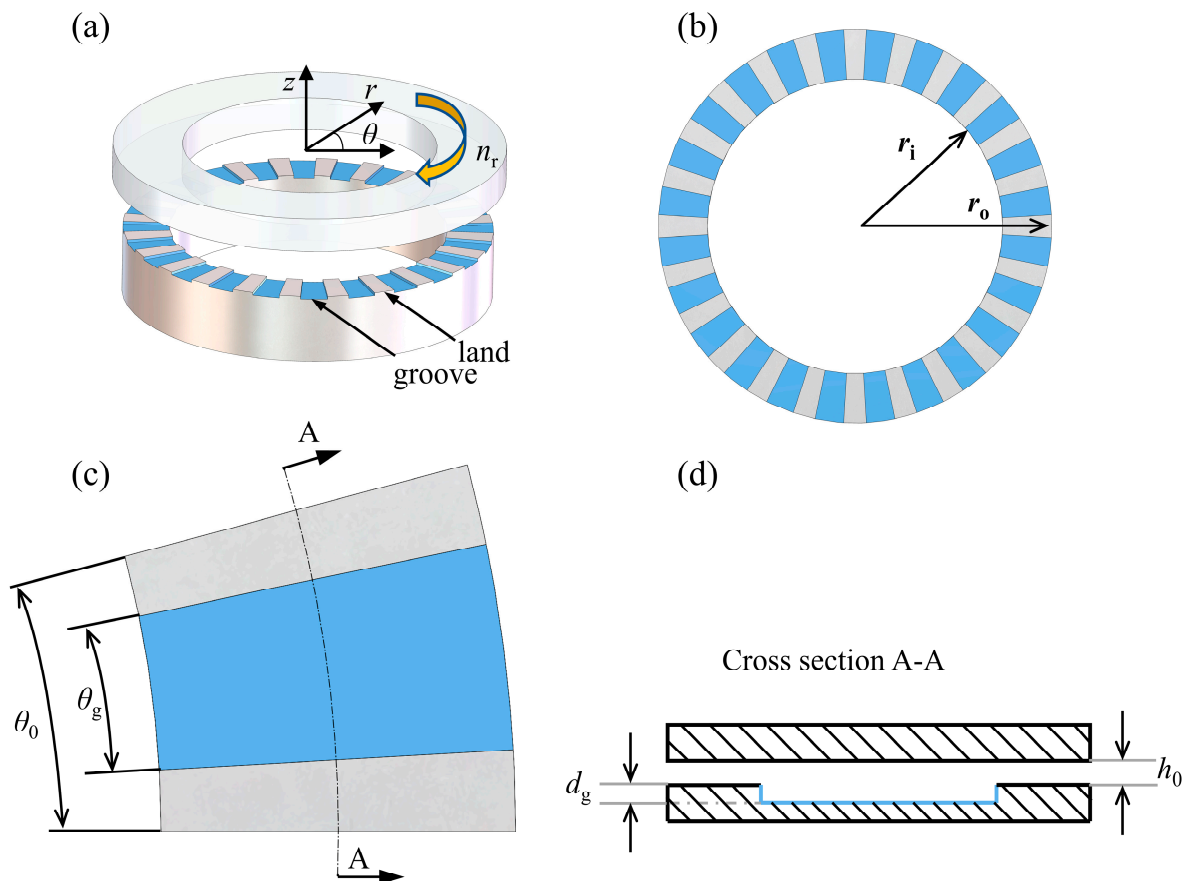


Figure 1. Physical model. (a) Smooth upper surface and a lower surface with straight-groove textures; (b) top view of the textured lower ring; (c) periodic sector; (d) cross section A-A.

The depth and area of surface texture significantly affect the internal flow behavior of surface texture. The texture depth ratio is formulated as follows:

$$\lambda_d = \frac{d_g}{h_0} \quad (1)$$

The area ratio is written as follows:

$$AR_g = \frac{\theta_g}{\theta_0} \quad (2)$$

2.2. Governing Equations

The body force and temperature change are not considered during the CFD calculation. The lubricating oil is assumed to be Newtonian incompressible fluid, and the viscosity of the fluid remains constant. The surface roughness and deformation are negligible.

Since the Reynolds number is below the threshold in the following results, the lubricating oil is supposed to be in a laminar flow state. The energy equation is not considered in this research.

Consequently, the CFD model solves the continuity equation, the momentum equation, and the volume fraction for the air phase. The mixture model is employed to model air–oil flow. When the local pressure is lower than p_c , the air dissolved in the oil is released.

The continuity equation is defined as

$$\frac{\partial}{\partial t}(\rho_m) + \nabla \cdot (\rho_m \vec{v}_m) = 0 \quad (3)$$

where ρ_m , the equation of which is written below, is the mixture density of air and oil:

$$\rho_m = \sum_{k=1}^2 \alpha_k \rho_k \quad (4)$$

where α_k is the volume fraction of phase k , and ρ_k is the density of phase k . \vec{v}_m is the mass-averaged velocity, and it is expressed as

$$\vec{v}_m = \frac{\sum_{k=1}^2 \alpha_k \rho_k \vec{v}_k}{\rho_m} \quad (5)$$

where \vec{v}_k is the velocity vector of phase k .

The momentum equation for the mixture of phase oil and gas is obtained as

$$\frac{\partial}{\partial t}(\rho_m \vec{v}_m) + \nabla(\rho_m \vec{v}_m \vec{v}_m) = -\nabla p + \nabla \cdot \left[\eta_m \left(\nabla \vec{v}_m + \nabla \vec{v}_m^T \right) \right] - \nabla \cdot \left(\sum_{k=1}^2 \alpha_k \rho_k \vec{v}_{dr,k} \vec{v}_{dr,k} \right) \quad (6)$$

where η_m , written below, is the dynamic viscosity of the mixture:

$$\eta_m = \sum_{k=1}^2 \alpha_k \eta_k \quad (7)$$

where $\vec{v}_{dr,k}$ is the drift velocity for phase k and is formulated as

$$\vec{v}_{dr,k} = \vec{v}_k - \vec{v}_m \quad (8)$$

The volume fraction equation for phase air is formulated as

$$\frac{\partial}{\partial t}(\alpha_{\text{air}} \rho_{\text{air}}) + \nabla(\alpha_{\text{air}} \rho_{\text{air}} \vec{v}_m) = R_f - R_c \quad (9)$$

where R_f and R_c are the mass transfer source terms related to the formation and collapse of the gas bubbles, respectively.

The Schenerr–Sauer model is employed to simulate cavitation due to its high efficiency, accuracy, and consistency for the theoretical model in this research and the experimental results presented in ref. [23]. This cavitation model is also used in refs. [31,32]. According to the Schenerr–Sauer model, the source terms in Equation (9) can be defined as

If $p \leq p_c$

$$R_f = \frac{\rho_{\text{oil}} \rho_{\text{air}}}{\rho_m} \alpha_{\text{air}} (1 - \alpha_{\text{air}}) \frac{3}{\Re_B} \sqrt{\frac{2}{3} \frac{p_{\text{air}} - p}{\rho_{\text{oil}}}} \quad (10)$$

If $p > p_c$

$$R_c = \frac{\rho_{\text{oil}} \rho_{\text{air}}}{\rho_m} \alpha_{\text{air}} (1 - \alpha_{\text{air}}) \frac{3}{\Re_B} \sqrt{\frac{2}{3} \frac{p - p_{\text{air}}}{\rho_{\text{oil}}}} \quad (11)$$

where \mathfrak{R}_B represents the radius of the bubble, and p_c represents the cavitation pressure, as mentioned in ref. [33], $\mathfrak{R}_B \approx 10^{-6}$ m. The relationship between the oil volume fraction and air volume fraction can be written as follows:

$$\alpha_{\text{oil}} + \alpha_{\text{air}} = 1 \quad (12)$$

The area ratio of cavitation is formulated as follows:

$$AR_c = \frac{S_c}{S_t} \quad (13)$$

where S_c is the cavitating area, and S_t represents the textured area.

The LCC of the oil film is defined as

$$w = \int_{r_i}^{r_o} \int_0^{\theta_0} (p - p_0) r dr d\theta \quad (14)$$

The steady-state flow behavior between the friction pair is focused on in this research. Thereafter, the steady-state continuity equation, momentum equation, and volume fraction equation are solved in the following cases.

2.3. Boundary Conditions and Mesh

Figure 2 displays the fluid computational domain. The upper surface is a no-slip rotational moving wall, while the lower surface is a no-slip stationary wall, with periodic boundary conditions on both circumferential sides. The surface at the inner radius is set as pressure inlet boundary condition, while the surface at the outer radius is set as pressure outlet boundary condition. The pressure on these two surfaces equals ambient pressure (101,325 Pa). As hexahedra elements are positive for tracking the cavitation region, ANSYS ICEM is employed to generate the entire hexahedral mesh. Figure 2b presents the mesh of the computational domain, and the aspect ratio of the mesh is controlled below 22.

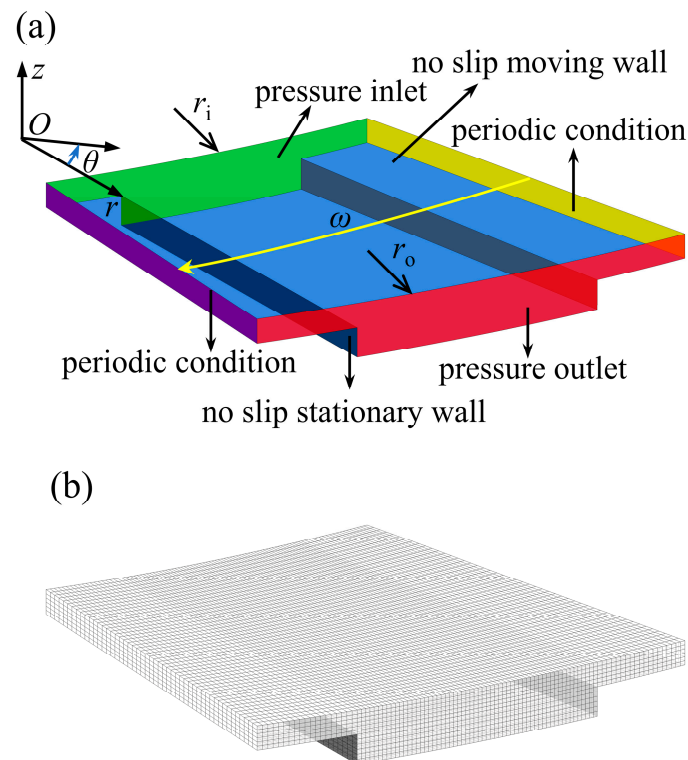


Figure 2. CFD model. (a) Boundary condition; (b) hexahedral mesh.

2.4. CFD Computation Details

Due to the superiority of parallel computation, the governing equations are solved by ANSYS FLUENT. The mixture model [33] is used to model multiphase flow between the friction pair. The finite volume method and the pressure-based solver are utilized to discretize the governing equations. The steady-state pressure–velocity coupling scheme SIMPLEC (SIMPLE-Consistent) is employed to solve the continuity and momentum equations iteratively. The gradients are calculated by the Green–Gauss Node-Based method. The PRESTO! scheme is employed for pressure spatial discretization, while the second-order upwind method is applied to momentum. The volume fraction equation is discretized using Compressive Interface Capturing Scheme for Arbitrary Meshes method. The under-relaxation of variables is employed to stabilize the convergence behavior of the iterations. When all scaled residuals are less than 10^{-4} , and the LCC remains unchanged, the convergence criterion of numerical calculation is satisfied.

3. Grid Sensitivity and Model Validation

Since the amount of mesh significantly impacts the accuracy and efficiency of the CFD model, it is imperative to validate the independence of the mesh. The effect of mesh amount on the LCC of oil is listed in Table 1. The grid number of oil thickness and that of texture depth are the same. The number of elements increases with the grid nodes to keep the mesh aspect ratio below 22. The LCC also changes with the mesh amount. When the grid nodes on the oil thickness and groove depth are 7 and 12, the load-carrying capacities are 2.15 N and 2.18 N, respectively. The differences between the LCC calculated by these two mesh schemes are about 0.9%, indicating that the mesh size effect can be ignored during accurate calculation when the number of grid nodes and the mesh amount are 7 and 1,444,752. Therefore, the grid nodes on the oil thickness and groove depth are set to 7, which can achieve the balance between computational efficiency and accuracy.

Table 1. Effect of mesh amount on the LCC.

| Grid Nodes on the Oil Thickness and Texture Depth | Number of Elements | LCC, N |
|---|--------------------|--------|
| 3 | 237,120 | 1.87 |
| 5 | 267,696 | 2.02 |
| 7 | 1,444,752 | 2.16 |
| 12 | 3,135,836 | 2.18 |

To verify the CFD model established in this paper, the numerical calculation in this research and the test result of the cavitation morphology in ref. [23] are compared and presented in Figure 3. The operating parameters utilized in ref. [23] are listed in Table 2. The green area in Figure 3a is the cavitation region calculated by the CFD simulation, which is a mixed region of oil and air. The bright zones in the groove texture area in Figure 3b is the cavitation region. The cavitation region morphology on the upper ring surface calculated by the CFD simulation is very consistent with that observed by the experiment. It reveals that the established CFD model is suitable for analyzing the internal flow behavior in surface texture.

Table 2. Operating parameters for comparison.

| Parameter | Value |
|--|--------|
| Unit cell angle, θ_0 (°) | 15 |
| Groove angle, θ_g (°) | 8.4 |
| Inner radius of the computational domain, r_i (mm) | 24 |
| Outer radius of the computational domain, r_o (mm) | 32 |
| Rotating speed of the upper ring, n_r (rpm) | 142 |
| Lubricating film thickness, h_0 (μm) | 8.4375 |

Table 2. Cont.

| Parameter | Value |
|---|-------------------------|
| Groove depth, d_g (μm) | 10.2 |
| Atmospheric pressure, p_0 (Pa) | 101,325 |
| Cavitating pressure, p_c (Pa) | 0.3×10^5 |
| Dynamic viscosity of the oil, η_{oil} (Pa·s) | 0.092 |
| Oil density, ρ_{oil} (kg/m^3) | 870 |
| Dynamic viscosity of the air, η_{air} (Pa·s) | 1.7894×10^{-5} |
| Air density, ρ_{air} (kg/m^3) | 1.225 |

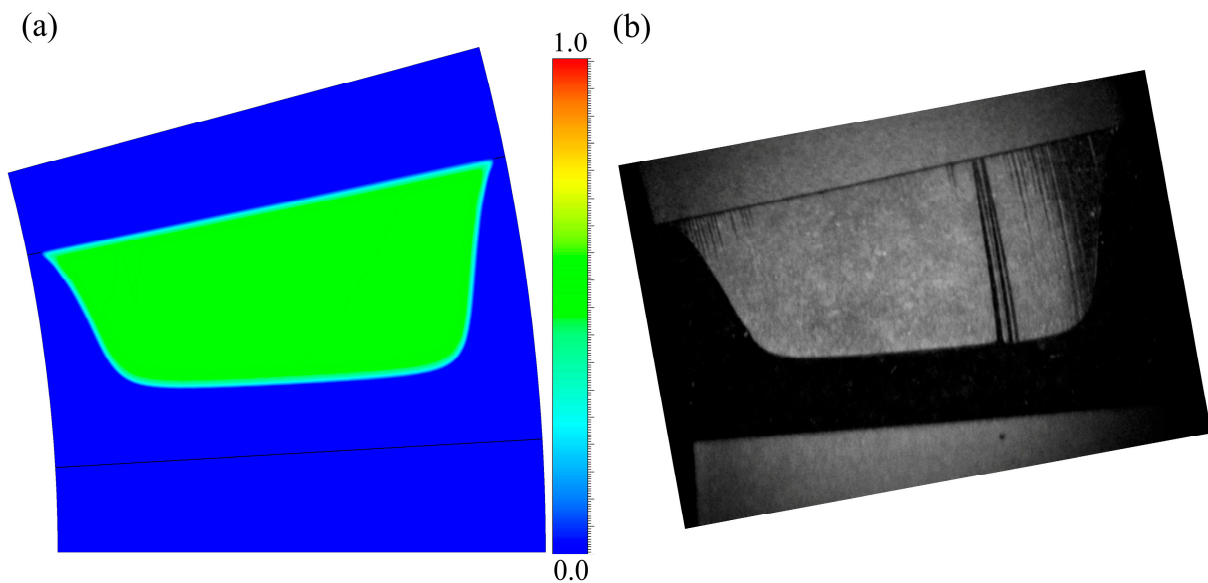


Figure 3. Comparison of cavitation morphology. (a) Air volume fraction on the upper ring surface calculated by CFD simulation; (b) cavitation region morphology observed by the experiment in ref. [23]. Reproduced with permission from ref. [23], © 2012, Springer Nature Tribology Letters.

4. Results and Discussion

Firstly, the three-dimensional flow behavior inside the straight-groove texture is analyzed using the operating parameters in Table 2. Then, the effect of Reynolds number, depth, and area ratio of the groove on the three-dimensional flow behavior in groove texture is investigated. Finally, the mechanism of texture on the tribological properties is summarized from the perspective of the flow behavior. Unless stated otherwise, the results refer to the operating values listed in Table 2.

4.1. Three-Dimensional Flow Field Characteristics

The plane at $r = 24$ mm, 26 mm, 28 mm, 30 mm, and 32 mm are intercepted from the fluid computational domain, and the corresponding streamline and air volume fraction α_{air} on these planes are extracted from the calculating results. The color of the streamline in Figure 4 represents the magnitude of velocity. The greyscale color map in the background indicates the air volume fraction; the white color is oil ($\alpha_{\text{air}} = 0$), while the black color represents air ($\alpha_{\text{air}} = 1$). There is no cavitation or vortex on plane $r = 24$ mm and plane $r = 32$ mm in Figure 4b,f, which are the planes at the boundaries of the inner and outer radii. The streamline and air volume fraction on plane $r = 26$ mm, 28 mm, and 30 mm are similar, and there exist vortices in both the upstream and downstream regions of the groove textures. The cavitation zone originates from the upstream divergent wedge and expands downstream along the angular velocity direction to the vicinity of the vortex zone. The cavitation zone and the vortex zone do not overlap.

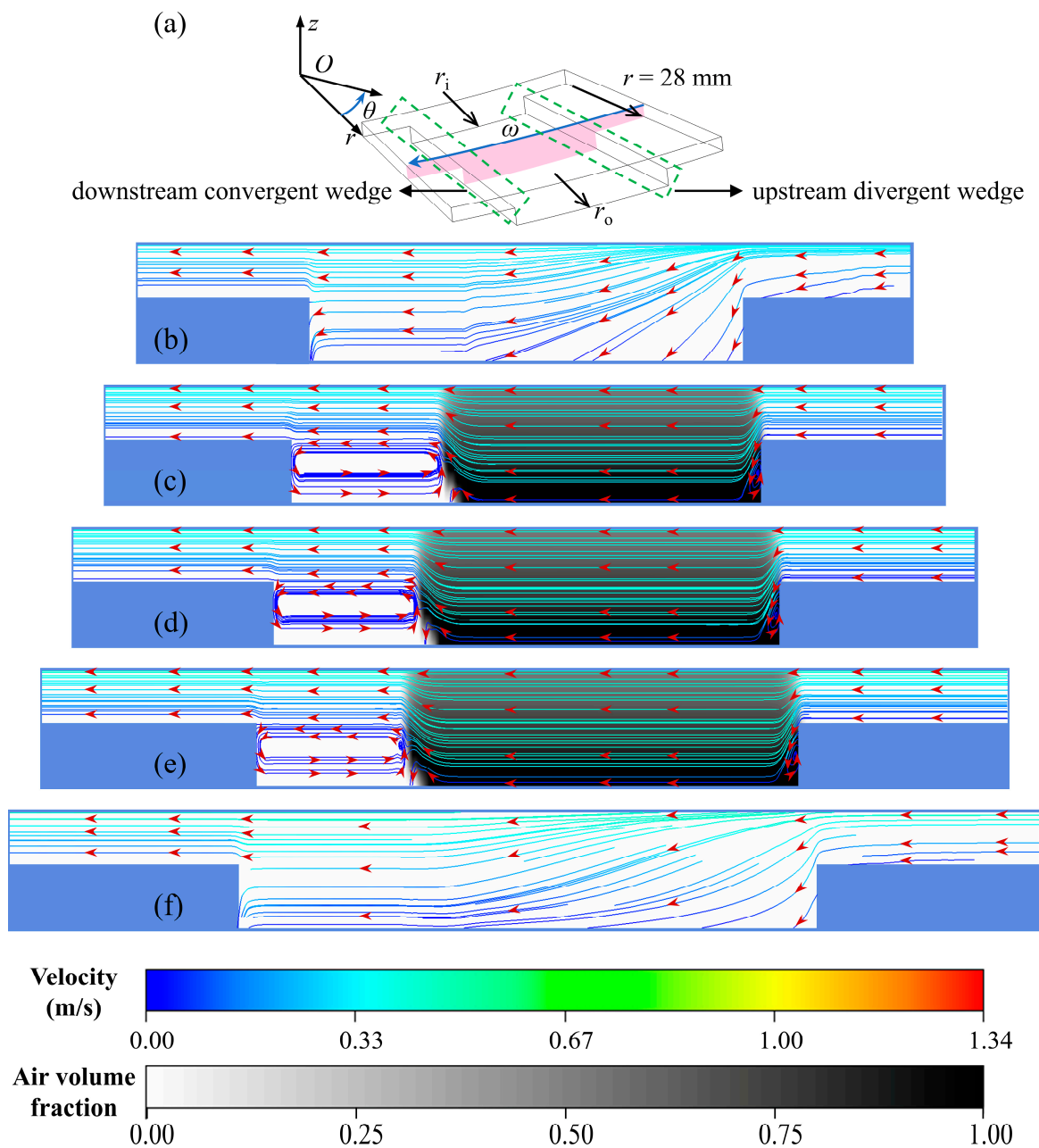


Figure 4. Streamline and air volume fraction on the circumferential planes with different r . (a) Schematic diagram of circumferential plane; (b) $r = 24$ mm; (c) $r = 26$ mm; (d) $r = 28$ mm; (e) $r = 30$ mm; (f) $r = 32$ mm.

Figure 5 presents the streamlines on plane $z = -7 \mu\text{m}$, $-3 \mu\text{m}$, $0 \mu\text{m}$, $3 \mu\text{m}$, and $7 \mu\text{m}$, and the corresponding pressure distributions on these planes are shown in Figure 6. The circumferential flow direction in the vortex zone is counterclockwise on plane $z = -7 \mu\text{m}$, while the directions of other streamlines in Figure 5c–f are all clockwise. The white line in Figure 6 is the boundary of cavitation. According to Figures 5 and 6, the circumferential velocity suddenly changes at the boundaries of cavitating zones, and the streamlines within the texture are distorted in the radial direction. The closer to the bottom of the texture, the more pronounced the distortion of the streamline. The distortion of the radial streamline indicates the presence of a significant side flow of lubricant at the pressure boundary. However, it is worth noting that previous two-dimensional CFD models, as described in the references, were conducted under the assumption of no side flow. This assumption may result in inaccurate calculation results. Therefore, there is a pressing need to investigate

the internal flow behavior of the surface texture using a three-dimensional CFD model to obtain more reliable and comprehensive results. Since the pressure at the zone near the upstream divergent wedge zone is lower than p_0 , oil at the inner and outer radius sections is sucked into the groove texture in the radial direction. On the other hand, the pressure in the zone near the downstream converge wedge is higher than p_0 , and oil at the inner and outer radius sections is extruded outward in the radial direction. The areas of cavitation zones and pressure distributions on different planes in Figure 6 are basically consistent.

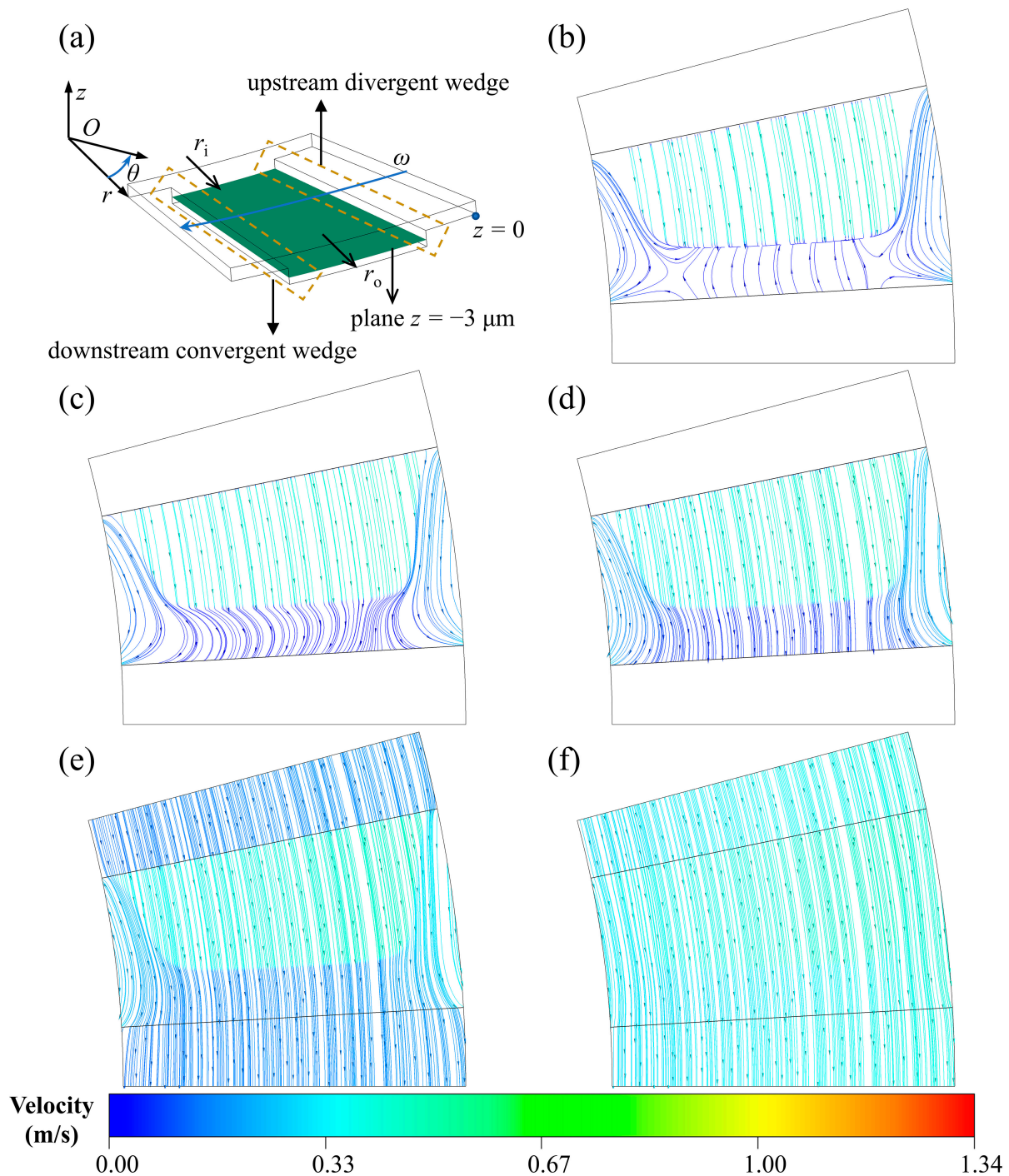


Figure 5. Streamline on the plane with different z . (a) Schematic diagram of the plane in the direction of z -axis; (b) $z = -7 \mu\text{m}$; (c) $z = -3 \mu\text{m}$; (d) $z = 0 \mu\text{m}$; (e) $z = 3 \mu\text{m}$; (f) $z = 7 \mu\text{m}$.

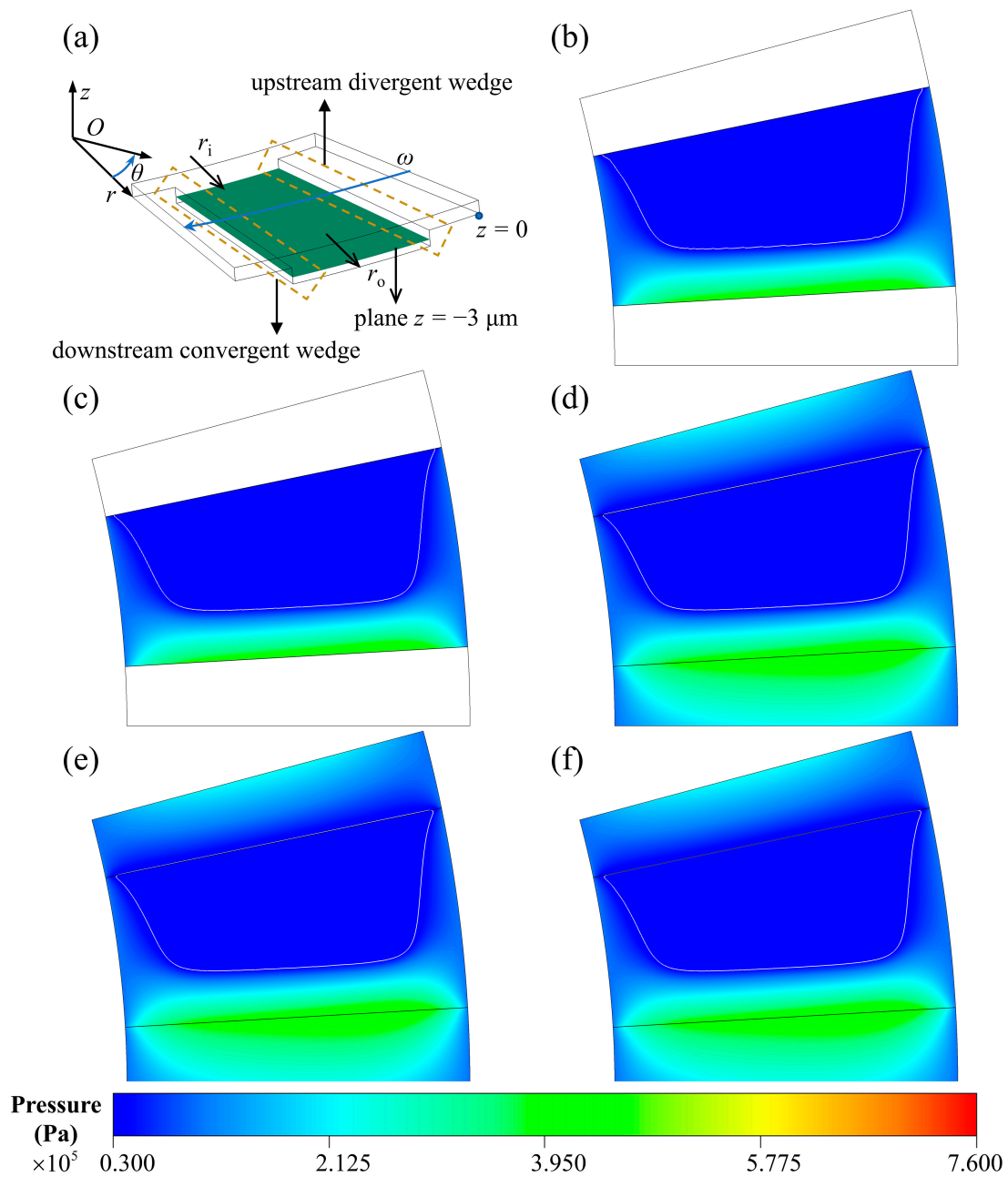


Figure 6. Pressure distribution on the plane with different z . (a) Schematic diagram of the plane in the direction of z -axis; (b) $z = -7 \mu\text{m}$; (c) $z = -3 \mu\text{m}$; (d) $z = 0 \mu\text{m}$; (e) $z = 3 \mu\text{m}$; (f) $z = 7 \mu\text{m}$.

4.2. Effect of Reynolds Number Re_o

The Reynolds number significantly affects flow behavior, which is defined in refs. [34,35] as follows:

$$Re_o = \frac{\rho_{oil}\omega r_o h_0}{\eta_{oil}} \quad (15)$$

where ω represents the angular velocity.

When the rotating speed is 100, 142, 200, 300, and 400 rpm, the corresponding Reynolds numbers are 0.0267, 0.0380, 0.0535, 0.0802, and 0.1070. These Reynolds numbers are less than the critical Reynolds number (1500) [34] for the transition from laminar to turbulent flow. As a result, the CFD simulation is conducted using these five Reynolds numbers in laminar flow.

As plane $r = 28$ mm is in the middle of the fluid domain in the radial direction, the streamline and air volume fraction α_{air} on this plane are extracted from the simulation results. Figure 7 shows apparent vortexes in both the upstream and downstream regions of the groove textures. The cavitating region originates from the divergent wedge of the upstream groove step and expands to the downstream region until it meets the vortex region. The pressure in the cavitating region is p_c , and a high-pressure area forms at the downstream convergent wedge. Due to the difference in pressure between the cavitating zone and the high-pressure zone, a vortex in the downstream region is formed. With the increase in the Reynolds number (Re_o), the cavitating area and upstream vortex area exhibit an increase in value, whereas the area of the downstream vortex decreases. The cavitation and downstream vortex zones are non-overlapping, which agrees with the conclusion proposed in ref. [29]. The downstream vortex restrains the expansion of the cavitation, and their areas show an inverse relationship in quantity.

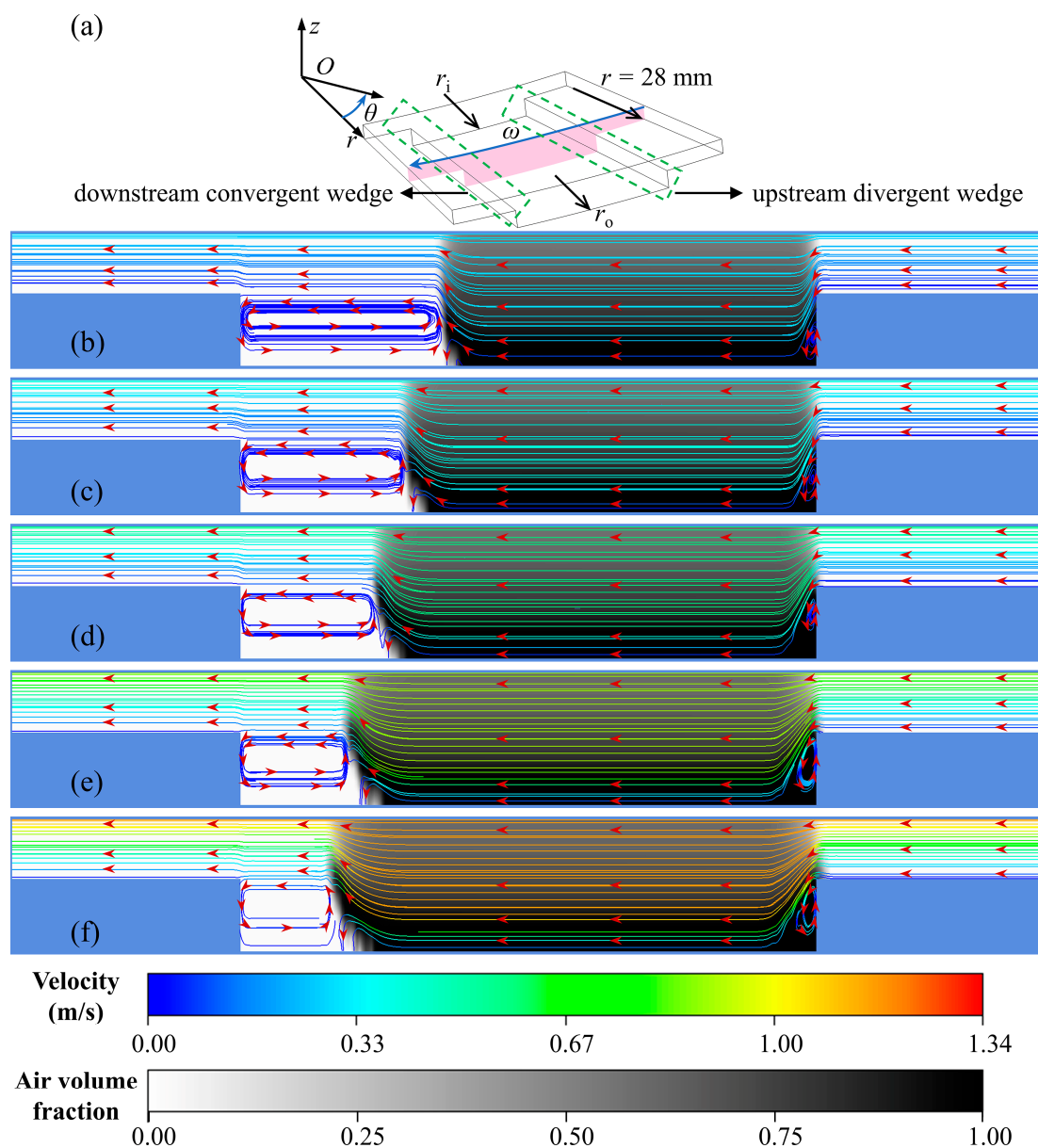


Figure 7. Streamline and air volume fraction on plane $r = 28$ mm. (a) plane $r = 28$ mm; (b) $Re_o = 0.0267$; (c) $Re_o = 0.0380$; (d) $Re_o = 0.0535$; (e) $Re_o = 0.0802$; (f) $Re_o = 0.1070$.

As presented in Figure 8a, a circular arc at $r = 28 \text{ mm}$, $z = -4 \text{ }\mu\text{m}$ is intercepted from the fluid computational domain, and the circumferential velocity v_c and air volume fraction α_{air} on this arc are extracted from the simulation results. Here, the circumferential velocity is positive in the counterclockwise direction. As presented in Figure 8b–f, the downstream boundary of the circumferential cavitating area inside the groove is where the circumferential velocity reaches zero. The upstream boundary of the circumferential cavitating zone is the upstream divergent wedge of the surface texture. Therefore, the position of the cavitation region in the groove is obtained by the boundary where the circumferential velocity is equal to 0 in the circumferential direction.

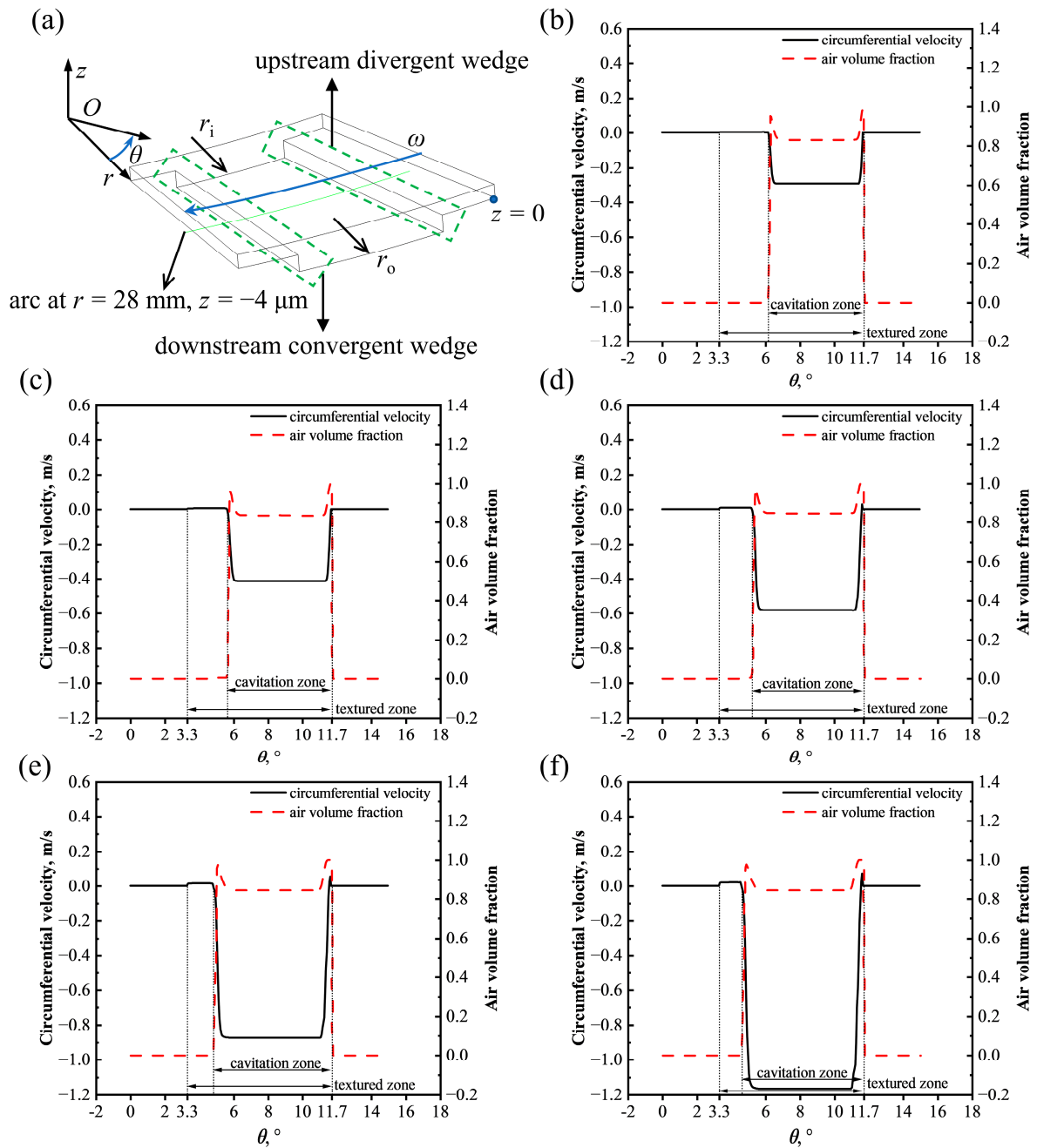


Figure 8. Circumferential velocity and air volume fraction on the circular arc at $r = 28 \text{ mm}$, $z = -4 \text{ }\mu\text{m}$. (a) Circular arc at $r = 28 \text{ mm}$, $z = -4 \text{ }\mu\text{m}$; (b) $Re_o = 0.0267$; (c) $Re_o = 0.0380$; (d) $Re_o = 0.0535$; (e) $Re_o = 0.0802$; (f) $Re_o = 0.1070$.

Figure 9a shows that a straight line at $\theta = 7.5^\circ$, $z = -4 \mu\text{m}$ is intercepted. Figure 9b–f present the radial velocity and air volume fraction on this line. Here, the radial velocity is positive along the inner to the outer radius direction. The location where the partial derivative of the radial velocity to r is equal to 0 and is the extremum point of the radial velocity, which coincides with the radial cavitating boundary. Therefore, the boundary of the radial cavitating region can be determined by the extremum points of the radial velocity.

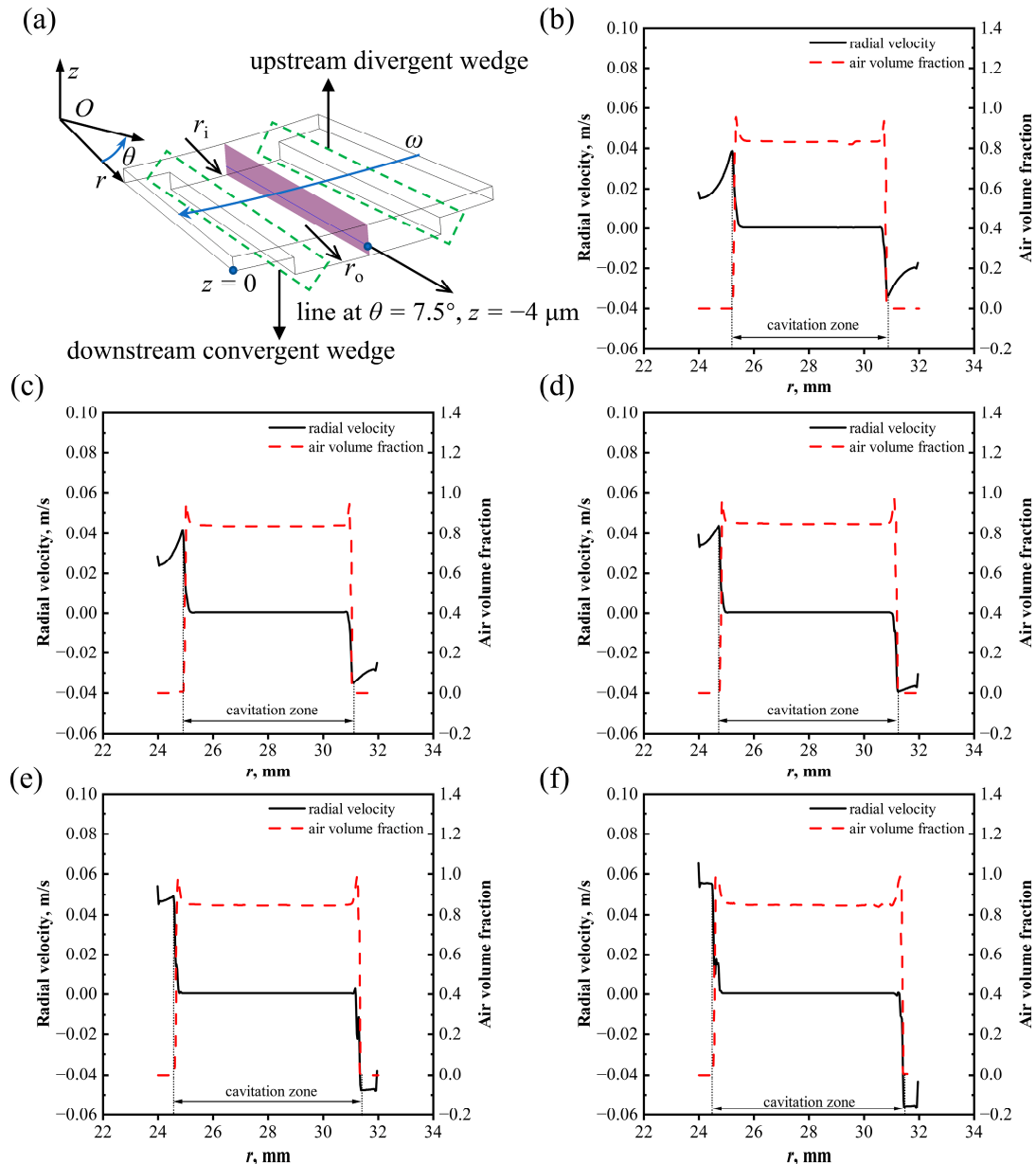


Figure 9. Radial velocity and air volume fraction on the line at $\theta = 7.5^\circ$, $z = -4 \mu\text{m}$. (a) The line at $\theta = 7.5^\circ$, $z = -4 \mu\text{m}$; (b) $Re_o = 0.0267$; (c) $Re_o = 0.0380$; (d) $Re_o = 0.0535$; (e) $Re_o = 0.0802$; (f) $Re_o = 0.1070$.

Owing to the pressure in the radial direction varying in different locations, the radial velocity v_r is generated. v_r increases along the inner to the outer radius direction, reaching the extremum point when the location of the cavitation area is reached and then decreasing rapidly to 0. The pressure on the outer radius plane surpasses that in the cavitation area, and driven by the pressure difference, lubricating oil near the outer radius surface flows into the groove texture. v_r decreases to the extremum value when the location of the cavitation area is reached, and then it increases rapidly to 0.

As shown in Figure 10a, the plane $z = -4 \mu\text{m}$ is intercepted from the computational domain. Figure 10b–f show the streamline on this plane, while Figure 11b–f show the corresponding pressure distribution. The pressure at the cavitation zone is p_c , which is less than the ambient pressure (p_0) at the inner and outer radius sections. Owing to the hydrodynamic effects, a high-pressure zone in Figure 11 forms at the downstream convergent wedge, which is higher than p_0 . The distorted streamline indicates that the lubricating oil near the cavitation zone is sucked into the groove texture in the radial direction. In contrast, the lubricating oil is extruded outward near the high-pressure zone. The origin of the suction and extrusion effects is the radial pressure difference. The smaller the Re_o , the more pronounced these suction and extrusion effects are and vice versa.

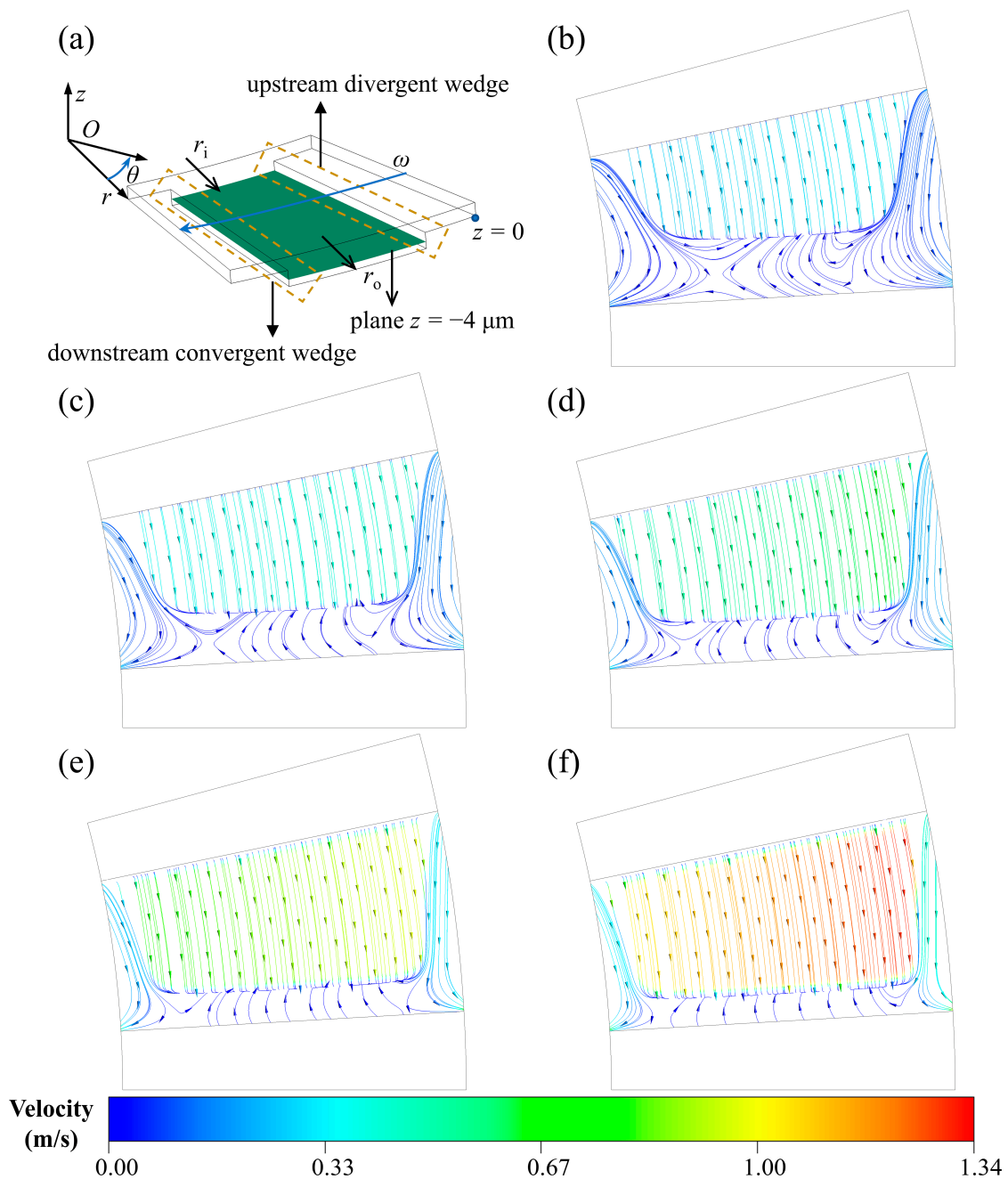


Figure 10. Streamline on plane $z = -4 \mu\text{m}$. (a) Plane $z = -4 \mu\text{m}$; (b) $Re_o = 0.0267$; (c) $Re_o = 0.0380$; (d) $Re_o = 0.0535$; (e) $Re_o = 0.0802$; (f) $Re_o = 0.1070$.

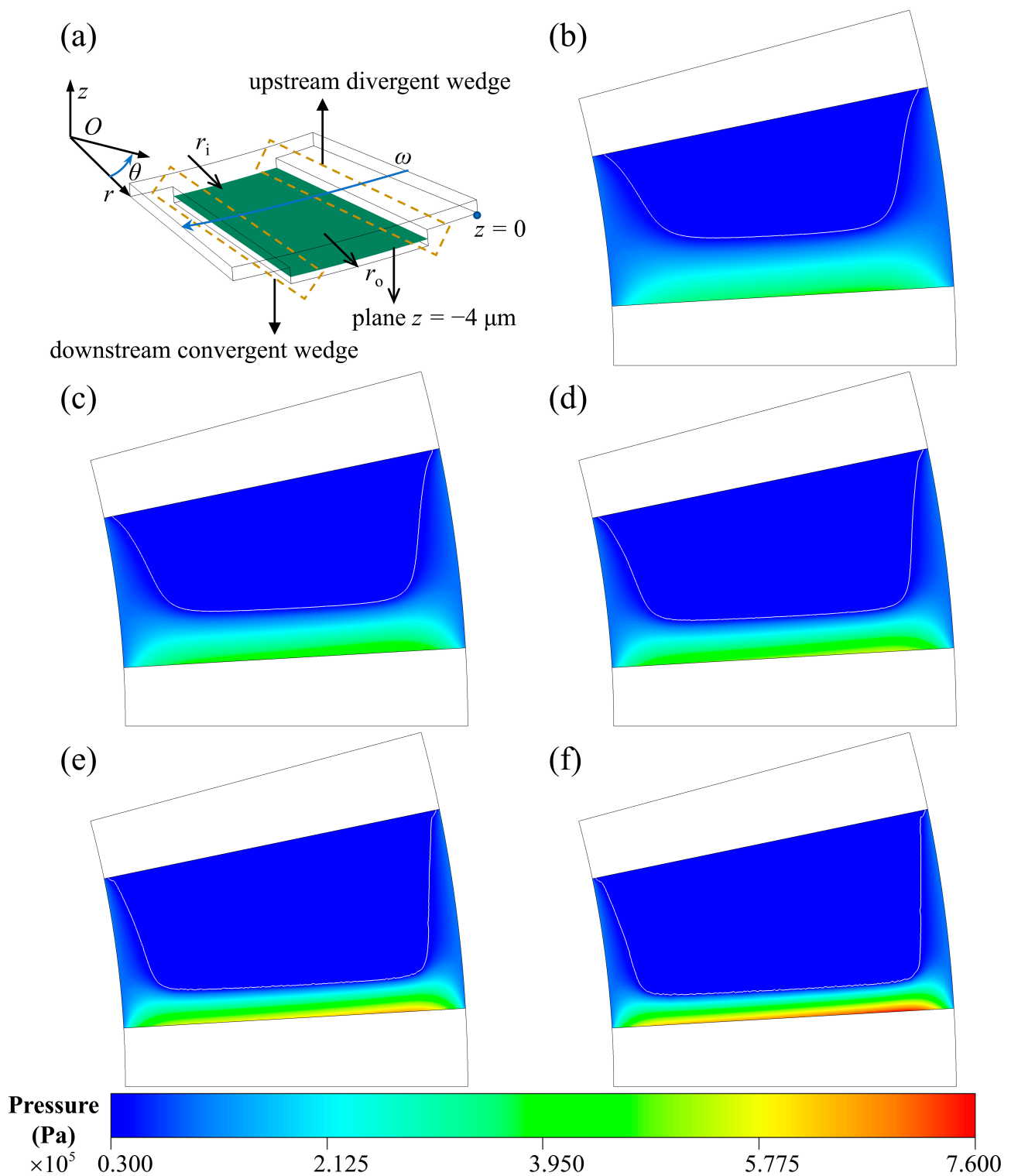


Figure 11. Pressure distribution on plane $z = -4 \mu\text{m}$. (a) Plane $z = -4 \mu\text{m}$; (b) $Re_o = 0.0267$; (c) $Re_o = 0.0380$; (d) $Re_o = 0.0535$; (e) $Re_o = 0.0802$; (f) $Re_o = 0.1070$.

Figure 12 shows the pressure nephogram on the upper ring. The area of the high-pressure region and cavitation region increases with the Reynolds number Re_o . Figure 13 presents the variation in the cavitating area ratio AR_c , LCC w , frictional force F_f , and frictional coefficient C_f with Re_o . These four parameters all increase with the Reynolds number. The hydrodynamic pressure effect at the downstream convergent wedge increases with Re_o . As shown in Figure 12, as Re_o increases, both the high-pressure area and maximum pressure

increase, leading to a higher LCC. As the rotating velocity increases, the circumferential velocity gradient in the film thickness direction also increases, leading to a rise in shear stress and frictional force. The variances in the LCC and the frictional force cause a slow increase in the frictional coefficient.

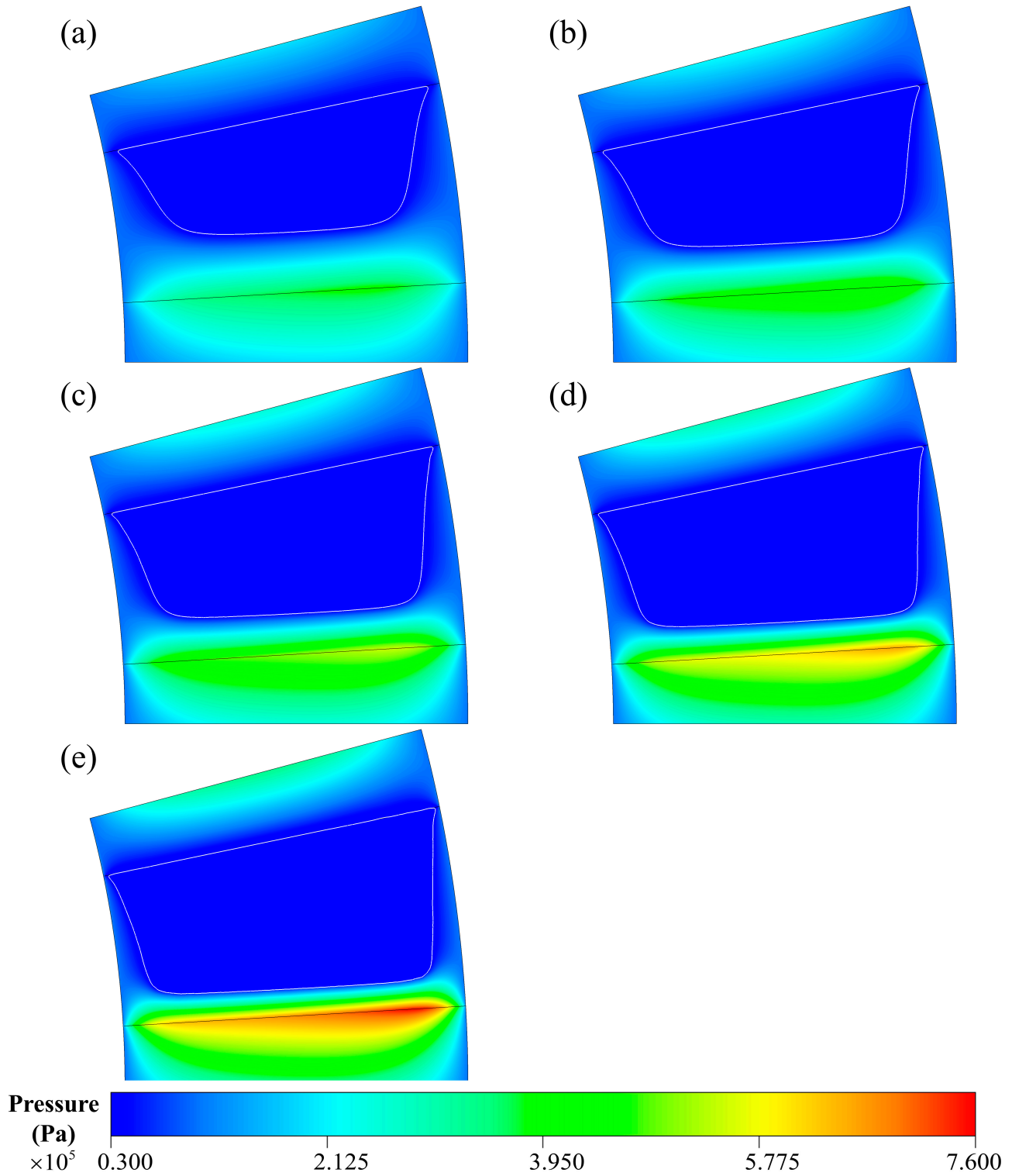


Figure 12. Pressure distribution on the upper surface. (a) $Re_o = 0.0267$; (b) $Re_o = 0.0380$; (c) $Re_o = 0.0535$; (d) $Re_o = 0.0802$; (e) $Re_o = 0.1070$.

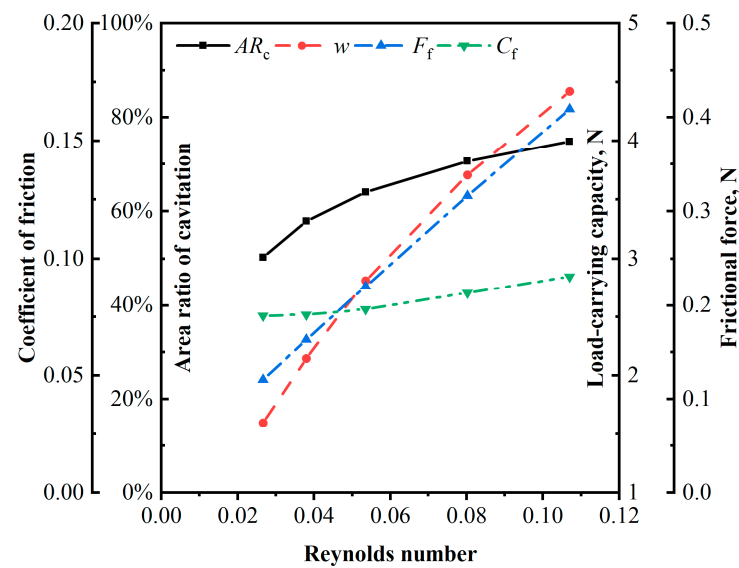


Figure 13. Cavitating area ratio AR_c , LCC w , frictional force F_f , and frictional coefficient C_f at different Re_o .

4.3. Effect of Depth Ratio λ_d

The texture depth significantly influences the internal flow behavior of the straight-groove texture. As mentioned in the previous sections, the same analyzing method is used. Planes and lines are intercepted in the circumferential direction and radial direction, respectively. The streamlines, air volume fraction, and velocity distribution on the planes and lines are extracted, and the effect of depth ratio on internal flow behavior is investigated.

When the depth of surface texture is 4 μm , 6 μm , 8.4375 μm , 11 μm , and 20 μm , the corresponding depth ratio λ_d is 0.48, 0.71, 1, 1.30, and 2.37. The simulation is then conducted under these five cases. The plane at $r = 28$ mm is intercepted, and the streamlines and air volume fraction on this surface are extracted from the calculation results, as shown in Figure 14. Cavitation occurs in all the cases. With an increase in the depth ratio, the cavitating area decreases. As shown in Figure 8b, the streamline is in order when the depth ratio is 0.48. There is no vortex in the upstream and downstream of the texture. With an increase in the depth ratio, vortices form both upstream and downstream of the texture. The existence of the vortex is beneficial for promoting the lubricating oil to flow into the texture and drain the lubricating oil out of the textured area. The vortex in surface texture functions as a micro-bearing to facilitate the flow of lubricating oil, which positively affects the lubricating property. When the depth ratio increases to 2.37, the downstream vortex in the groove texture exceeds the land area of the lower ring. The downstream vortex will inhibit the lubricant flowing out of the groove texture area, as shown in Figure 14f. Moreover, the larger the vortex area, the more kinetic energy is dissipated, negatively affecting the hydrodynamic effect. The vortex also suppresses the cavitation in the downstream of the groove texture.

A circular arc at $r = 28$ mm in Figure 15a is intercepted from the fluid computational domain. Owing to the different depth ratios of groove texture in these five cases, the z -coordinates of these cases are different. When the relationship between the cavitation zone and velocity in the circumferential and radial directions are analyzed in Sections 4.1 and 4.3, a circular arc and straight line are intercepted from the plane $z = -4$ μm to maintain mutual consistency. The groove depth in the first case is 4 μm , so the circumferential and radial velocities are equal to 0 in the plane $z = -4$ μm . According to the above reasons, the data in Figures 15b, 16b and 17b are extracted from $z = -2$ μm .

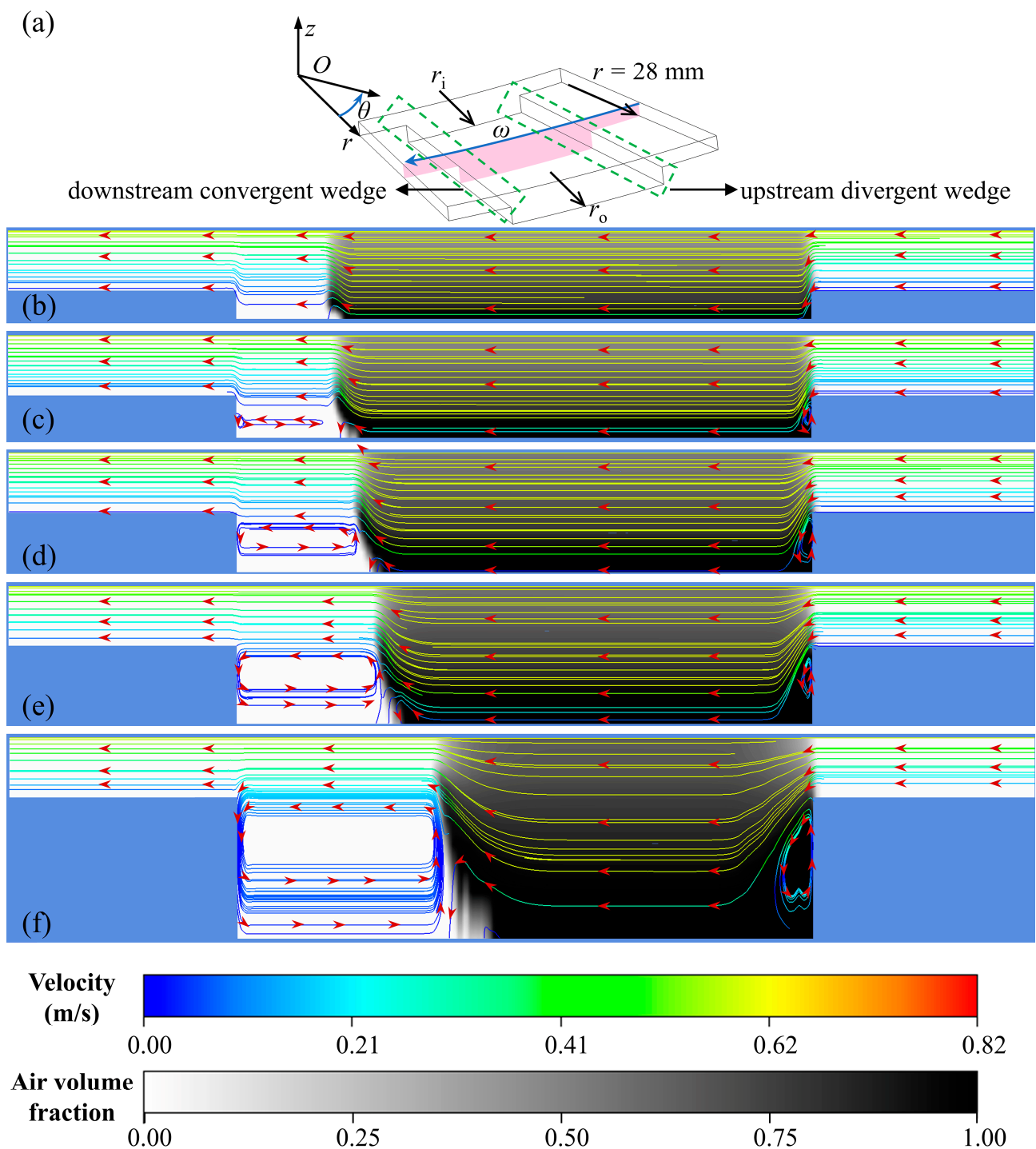


Figure 14. Streamline and air volume fraction on plane $r = 28$ mm. (a) Plane $r = 28$ mm; (b) $\lambda_d = 0.48$; (c) $\lambda_d = 0.71$; (d) $\lambda_d = 1$; (e) $\lambda_d = 1.30$; (f) $\lambda_d = 2.37$.

The downstream boundaries of the circumferential cavitation zone in Figure 15b,f are the extremum points of the circumferential velocities inside the textured zone. As presented in Figure 15c–e, the θ -coordinate where the downstream circumferential velocity equals 0 is the downstream boundary of the circumferential cavitation area inside the textured zone. The upstream boundary of the circumferential cavitation zone is the upstream step edge of surface texture. Therefore, the θ -coordinate of the cavitation region in the textured area can be determined by the boundary where the circumferential velocity is equal to 0 or the extremum point.

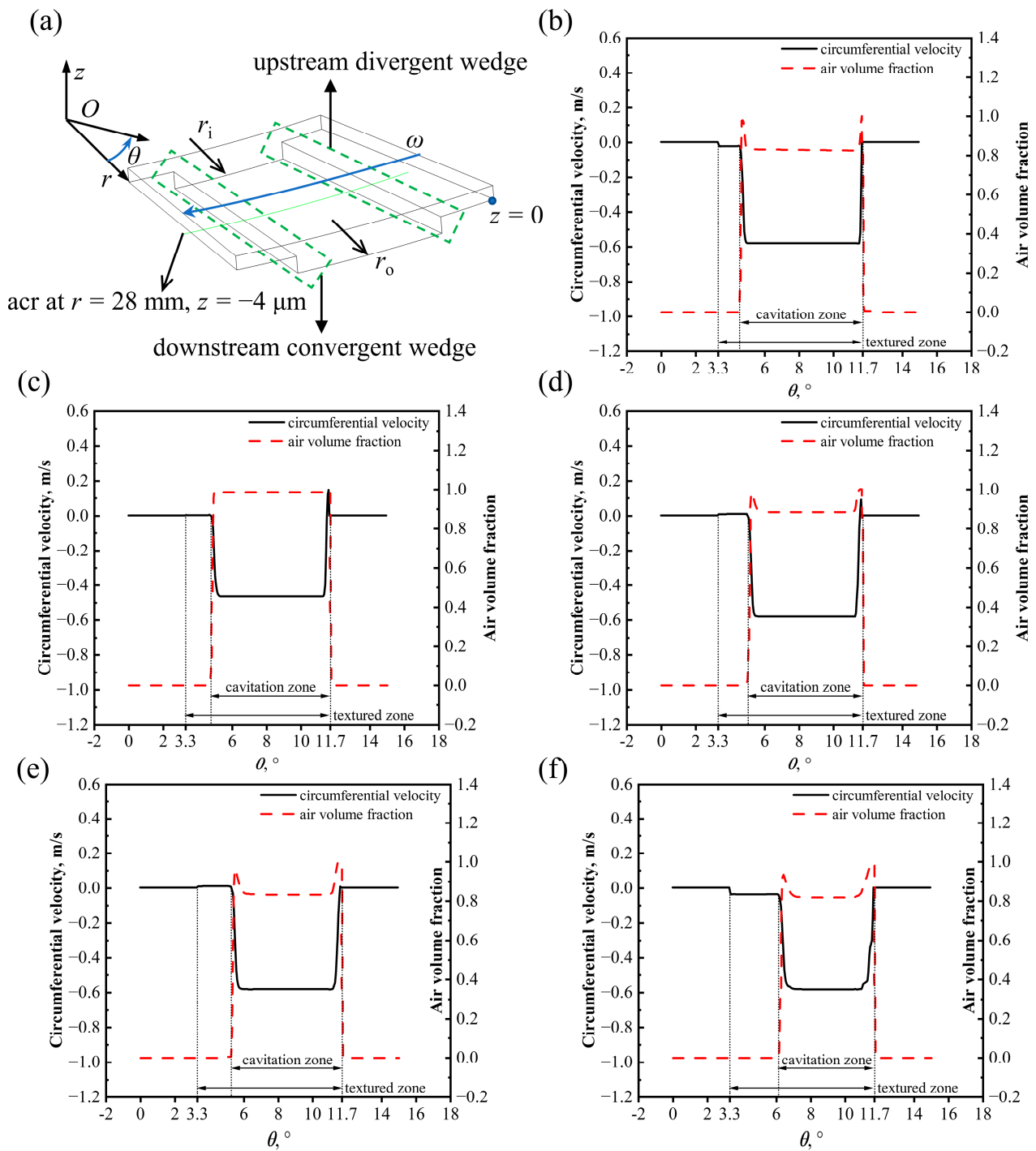


Figure 15. Circumferential velocity and air volume fraction on the circular arc at $r = 28$ mm. (a) Circular arc at $r = 28$ mm; (b) $\lambda_d = 0.48, z = -2$ μ m; (c) $\lambda_d = 0.71, z = -4$ μ m; (d) $\lambda_d = 1, z = -4$ μ m; (e) $\lambda_d = 1.30, z = -4$ μ m; (f) $\lambda_d = 2.37, z = -4$ μ m.

A straight line at $\theta = 7.5^\circ, z = -4$ μ m is intercepted. Figure 16a,c–f present the radial velocity and air volume fraction on this line, while Figure 16b shows these parameters on the line at $\theta = 7.5^\circ, z = -2$ μ m. The r -coordinate where the partial derivative of the radial velocity to r is equal to 0 is the extremum point of the radial velocity, which coincides with the radial boundary of the cavitating region. Therefore, the boundary of the radial cavitation region can be determined by the extremum points of the radial velocity.

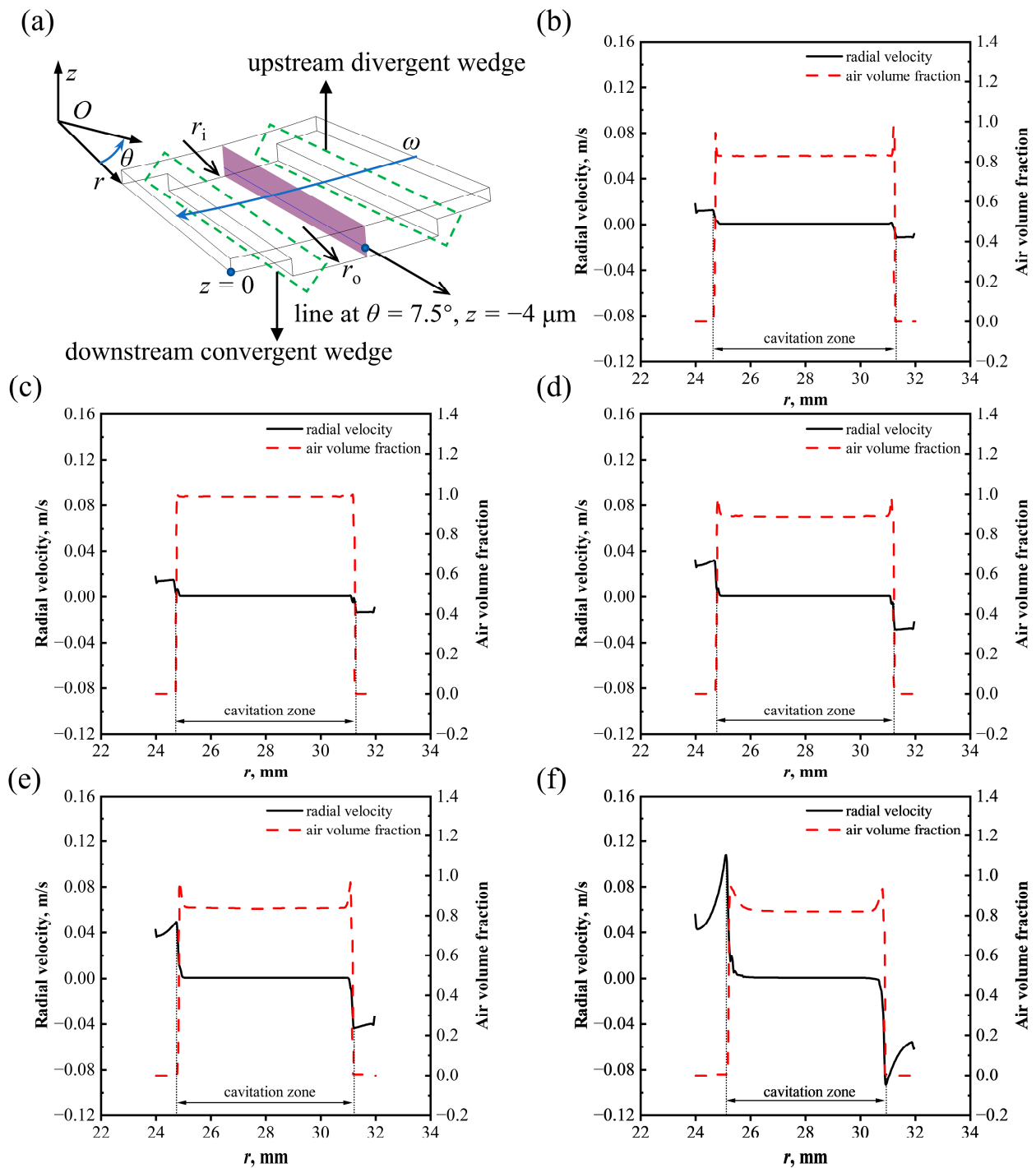


Figure 16. Radial velocity and air volume fraction on the line at $\theta = 7.5^\circ$. (a) The line at $\theta = 7.5^\circ$, $z = -4 \mu\text{m}$; (b) $\lambda_d = 0.48$, $z = -2 \mu\text{m}$; (c) $\lambda_d = 0.71$, $z = -4 \mu\text{m}$; (d) $\lambda_d = 1$, $z = -4 \mu\text{m}$; (e) $\lambda_d = 1.30$, $z = -4 \mu\text{m}$; (f) $\lambda_d = 2.37$, $z = -4 \mu\text{m}$.

Plane $z = -4 \mu\text{m}$ in Figure 17a is intercepted from the CFD model. Figure 17c–f shows the streamline on this plane, and Figure 17b shows the streamline on the plane at $z = -2 \mu\text{m}$. The streamlines converge radially in the area near the cavitation, which results in a suction effect [36]. Meanwhile, the streamlines diverge radially near the high-pressure zone, pushing the lubricating oil outward. The bigger the λ_d , the more noticeable these effects are and vice versa.

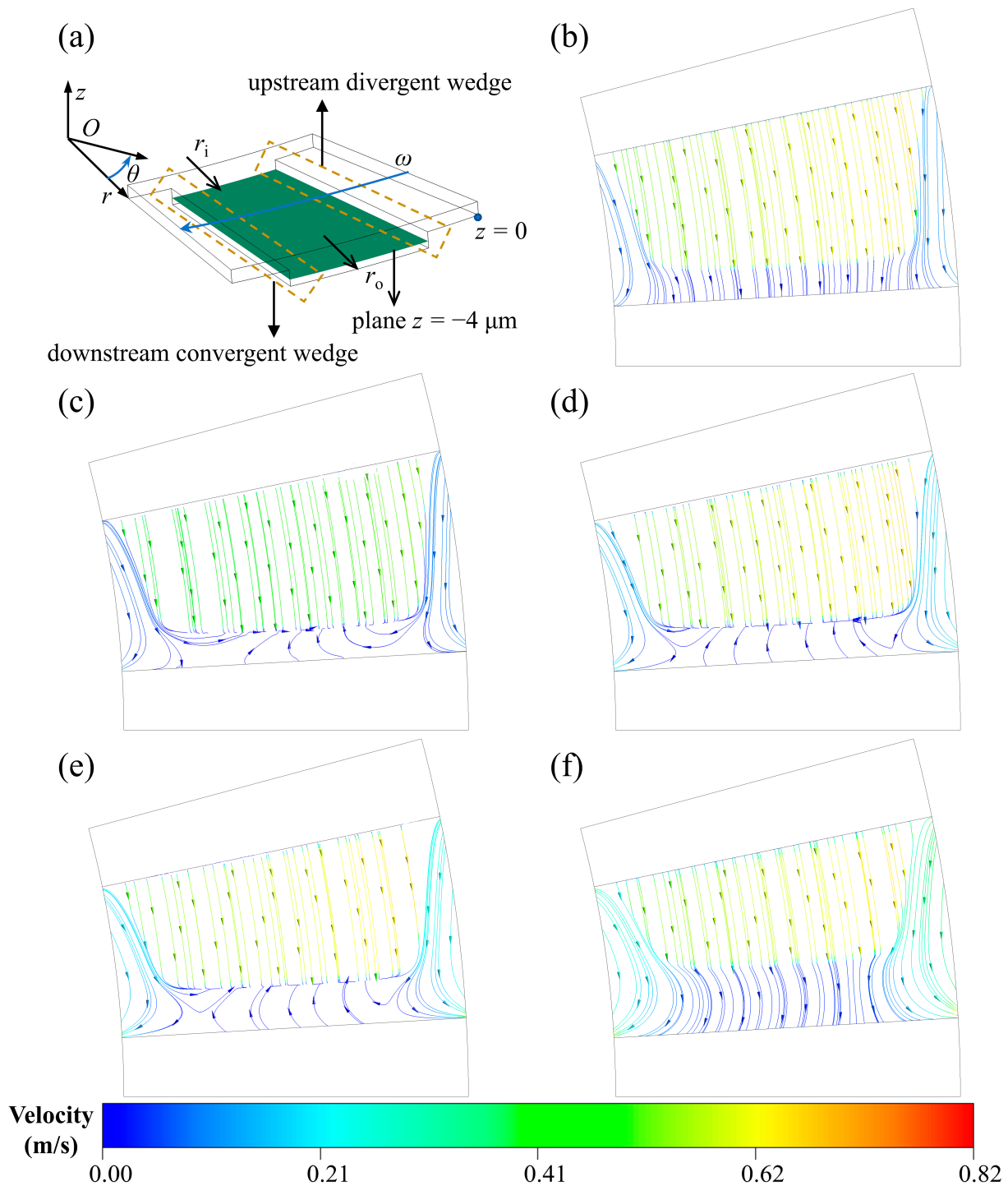


Figure 17. Streamline on plane $z = -4 \mu\text{m}$. (a) Plane $z = -4 \mu\text{m}$; (b) $\lambda_d = 0.48$, $z = -2 \mu\text{m}$; (c) $\lambda_d = 0.71$, $z = -4 \mu\text{m}$; (d) $\lambda_d = 1$, $z = -4 \mu\text{m}$; (e) $\lambda_d = 1.30$, $z = -4 \mu\text{m}$; (f) $\lambda_d = 2.37$, $z = -4 \mu\text{m}$.

Figure 18 shows the pressure nephogram on the upper ring. With an increase in the depth ratio, the cavitating area reduces while the maximum pressure and high-pressure zone area initially increase before decreasing. As shown in Figure 19, changes in the above parameters initially increase the LCC, followed by a decrease, while the frictional force stays relatively constant before gradually increasing. The fluctuating trends of LCC and frictional force cause the friction coefficient to initially decrease and then increase. When the depth ratio λ_d equals 1.30, the LCC is the largest, and the frictional coefficient is the minimum among these five cases.

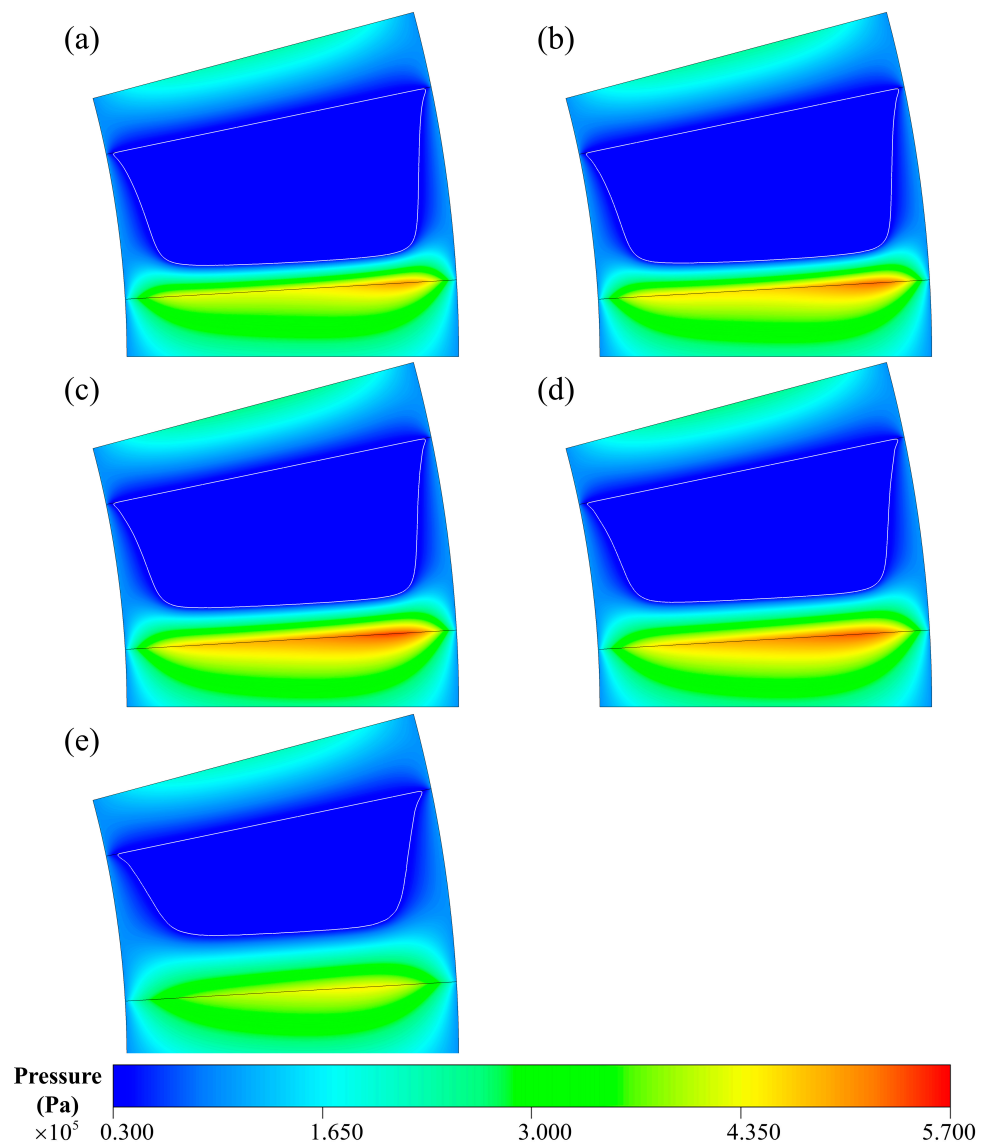


Figure 18. Pressure distribution on the upper surface. (a) $\lambda_d = 0.48$; (b) $\lambda_d = 0.71$; (c) $\lambda_d = 1$; (d) $\lambda_d = 1.30$; (e) $\lambda_d = 2.37$.

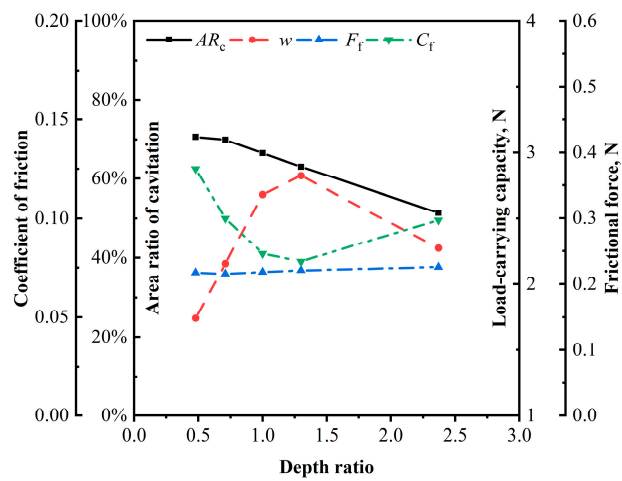


Figure 19. Cavitating area ratio AR_c , LCC w , frictional force F_f , and frictional coefficient C_f at different depth ratios.

According to the above analysis, the LCC of the oil film is influenced by the cavitating area, high-pressure area, and maximum pressure simultaneously. The cavitation zone is composed of phase oil and air, so the viscosity of the cavitation zone is less than that of the lubricating oil. Accordingly, the larger the cavitation area, the smaller the shear stress and frictional force.

4.4. Effect of Area Ratio AR_g

This section examines the impact of texture area ratio on internal flow behavior. CFD simulations are conducted for area ratios of 0.2, 0.3, 0.4, 0.56, and 0.7. The streamline and air volume fraction on plane $r = 28$ mm are shown in Figure 20. Vortexes are generated in upstream and downstream regions within the groove texture, and cavitation occurs in the texture in all these cases. It can be found that the vortex and cavitation region areas increase with the texture area ratio.

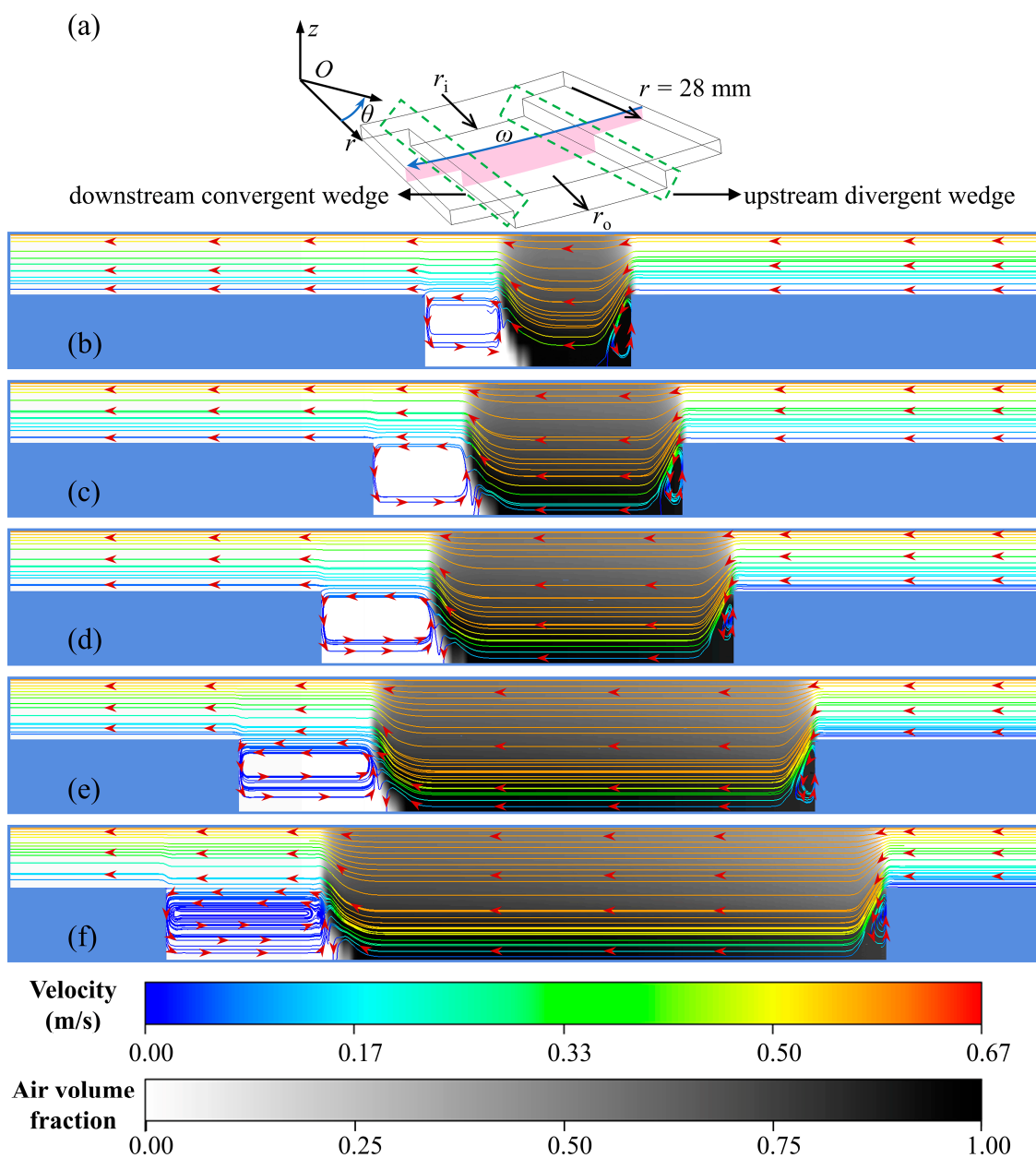


Figure 20. Streamline and air volume fraction on plane $r = 28$ mm. (a) Plane $r = 28$ mm; (b) $AR_g = 0.2$; (c) $AR_g = 0.3$; (d) $AR_g = 0.4$; (e) $AR_g = 0.56$; (f) $AR_g = 0.7$.

The circumferential velocity v_c and air volume fraction α_{air} on the circular arc at $r = 28 \text{ mm}$, $z = -4 \text{ }\mu\text{m}$ are presented in Figure 21. The θ -coordinate of the cavitation region in the groove texture can be defined by the boundary where the circumferential velocity is equal to 0, which is consistent with the previous section.

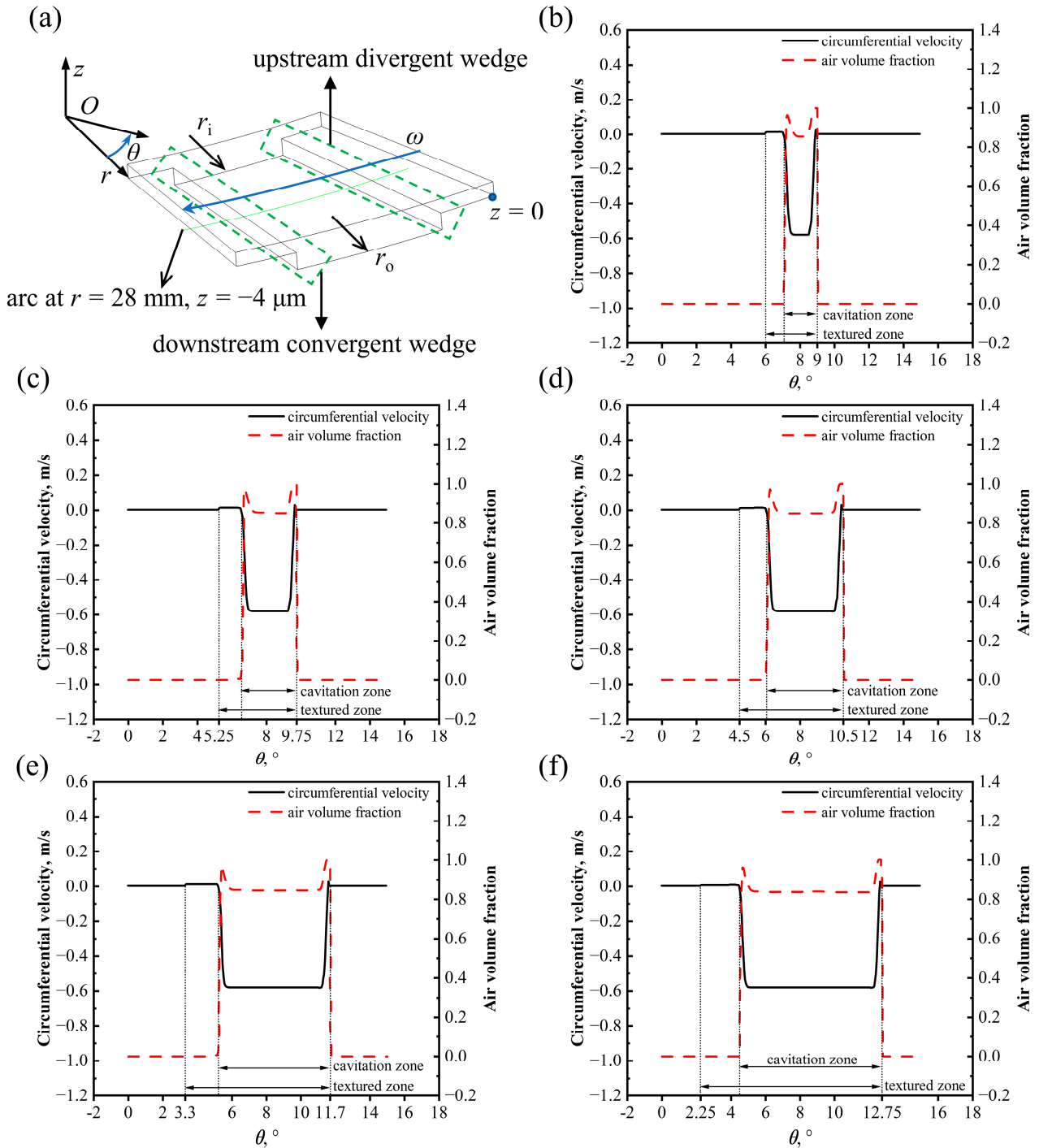


Figure 21. Circumferential velocity and air volume fraction on the circular arc at $r = 28 \text{ mm}$, $z = -4 \text{ }\mu\text{m}$. (a) Circular arc at $r = 28 \text{ mm}$, $z = -4 \text{ }\mu\text{m}$; (b) $AR_g = 0.2$; (c) $AR_g = 0.3$; (d) $AR_g = 0.4$; (e) $AR_g = 0.56$; (f) $AR_g = 0.7$.

Figure 22 shows the radial velocity and air volume fraction on the line at $\theta = 7.5^\circ$, $z = -4 \text{ }\mu\text{m}$. As investigated in the previous section, the boundary of the radial cavitation region can be determined by the extremum points of the radial velocity.

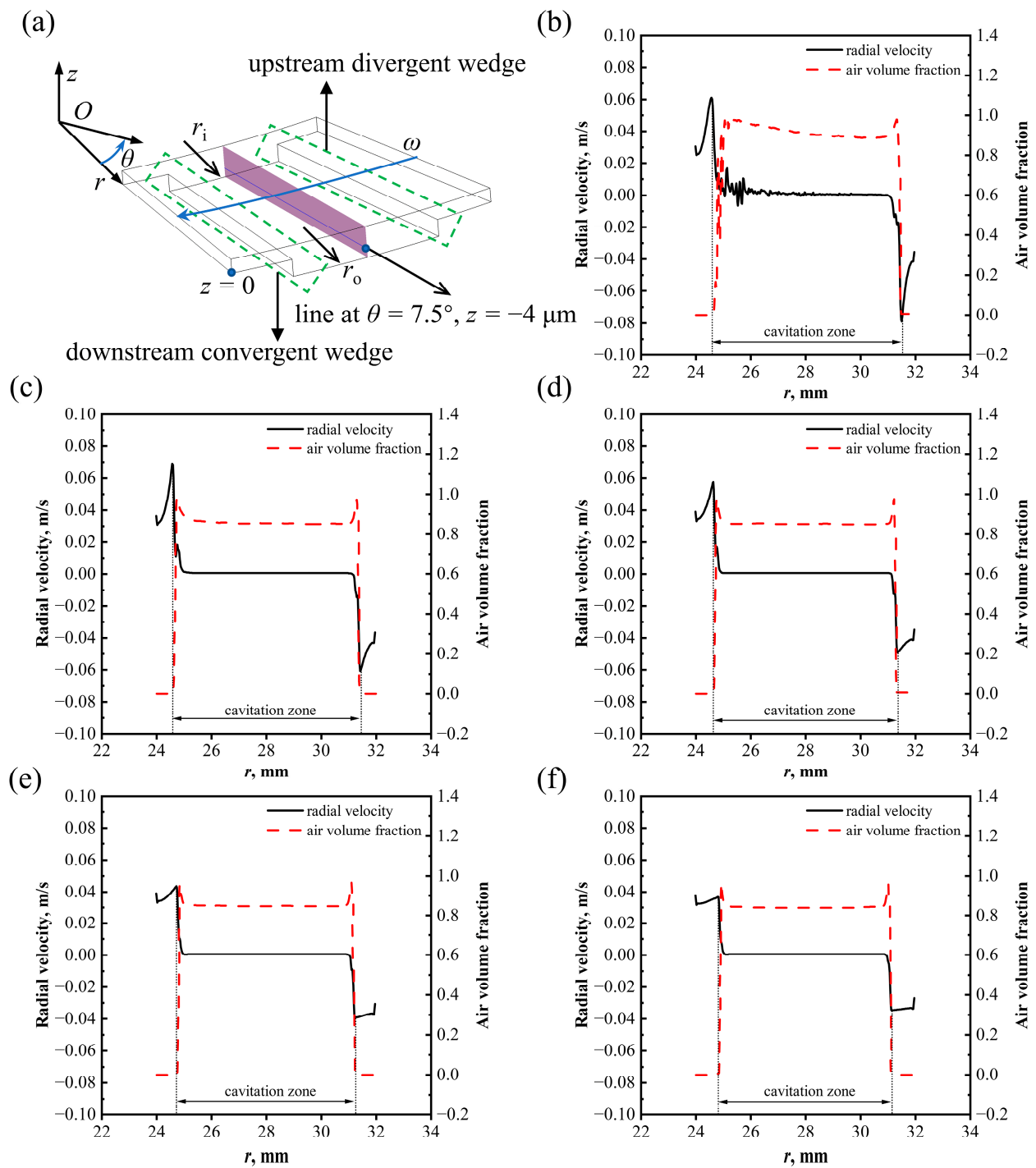


Figure 22. Radial velocity and air volume fraction on the line at $\theta = 7.5^\circ$, $z = -4 \mu\text{m}$. (a) The line at $\theta = 7.5^\circ$, $z = -4 \mu\text{m}$; (b) $AR_g = 0.2$; (c) $AR_g = 0.3$; (d) $AR_g = 0.4$; (e) $AR_g = 0.56$; (f) $AR_g = 0.7$.

Figure 23 shows the streamline and pressure distribution on plane $z = -4 \mu\text{m}$ for different texture area ratios. The streamlines are distorted in the radial direction, which converge radially in the area near the cavitation. The streamlines diverge radially near the high-pressure zone. Therefore, the lubricating oil is sucked into and pushed out of the textured zone, and these two effects exist simultaneously. The bigger the AR_g , the more pronounced these effects are and vice versa.

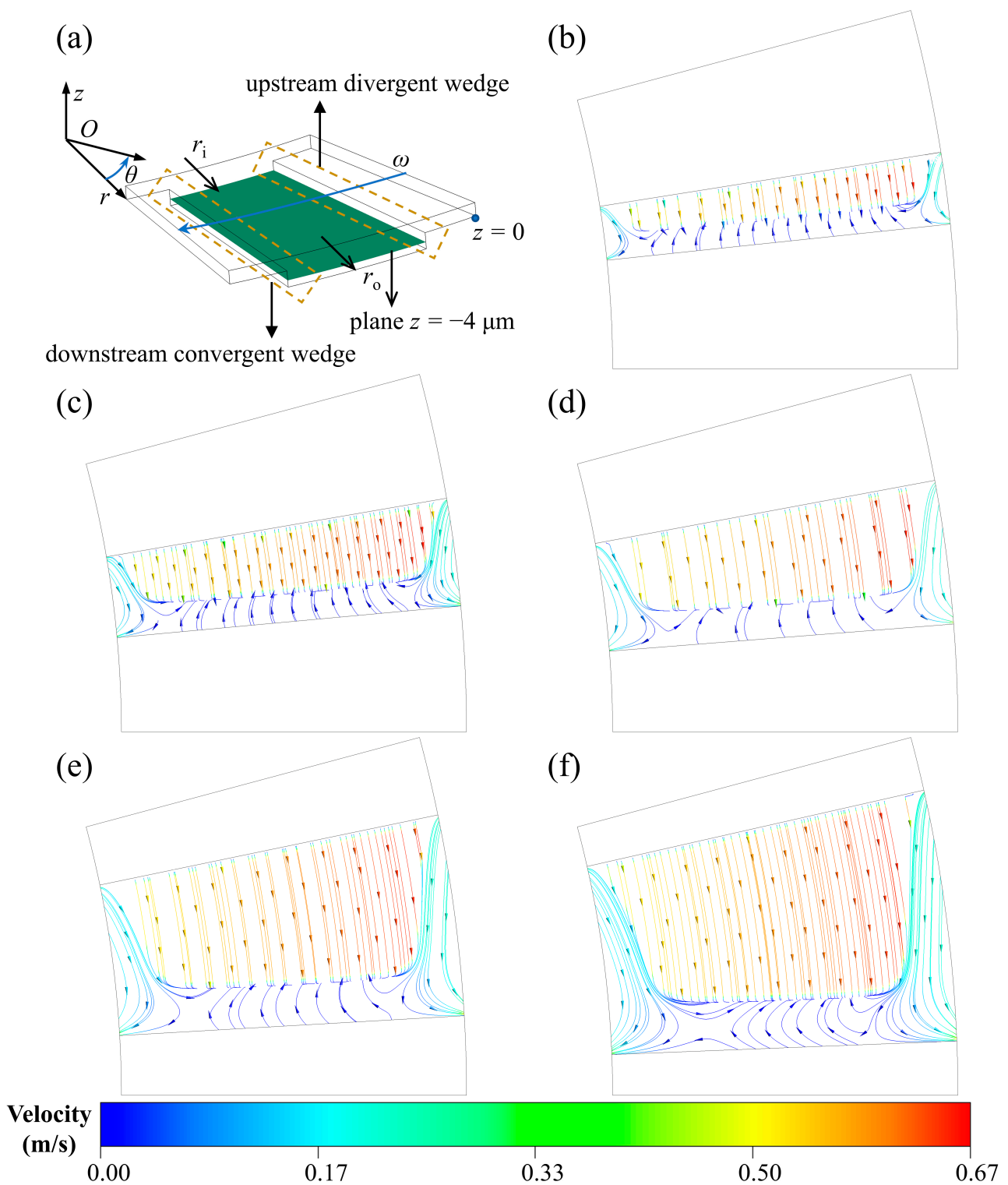


Figure 23. Streamline on plane $z = -4 \mu\text{m}$. (a) Plane $z = -4 \mu\text{m}$; (b) $AR_g = 0.2$; (c) $AR_g = 0.3$; (d) $AR_g = 0.4$; (e) $AR_g = 0.56$; (f) $AR_g = 0.7$.

Figure 24 shows the pressure nephogram on the upper ring. With an increase in the texture ratio, the cavitation area, the high-pressure area, and the maximum pressure. Since the pressure in the cavitating zone is the cavitating pressure (p_c), according to the formula of the LCC, the LCC is at a maximum when the cavitating area, high-pressure area, and maximum pressure reach a certain balance.

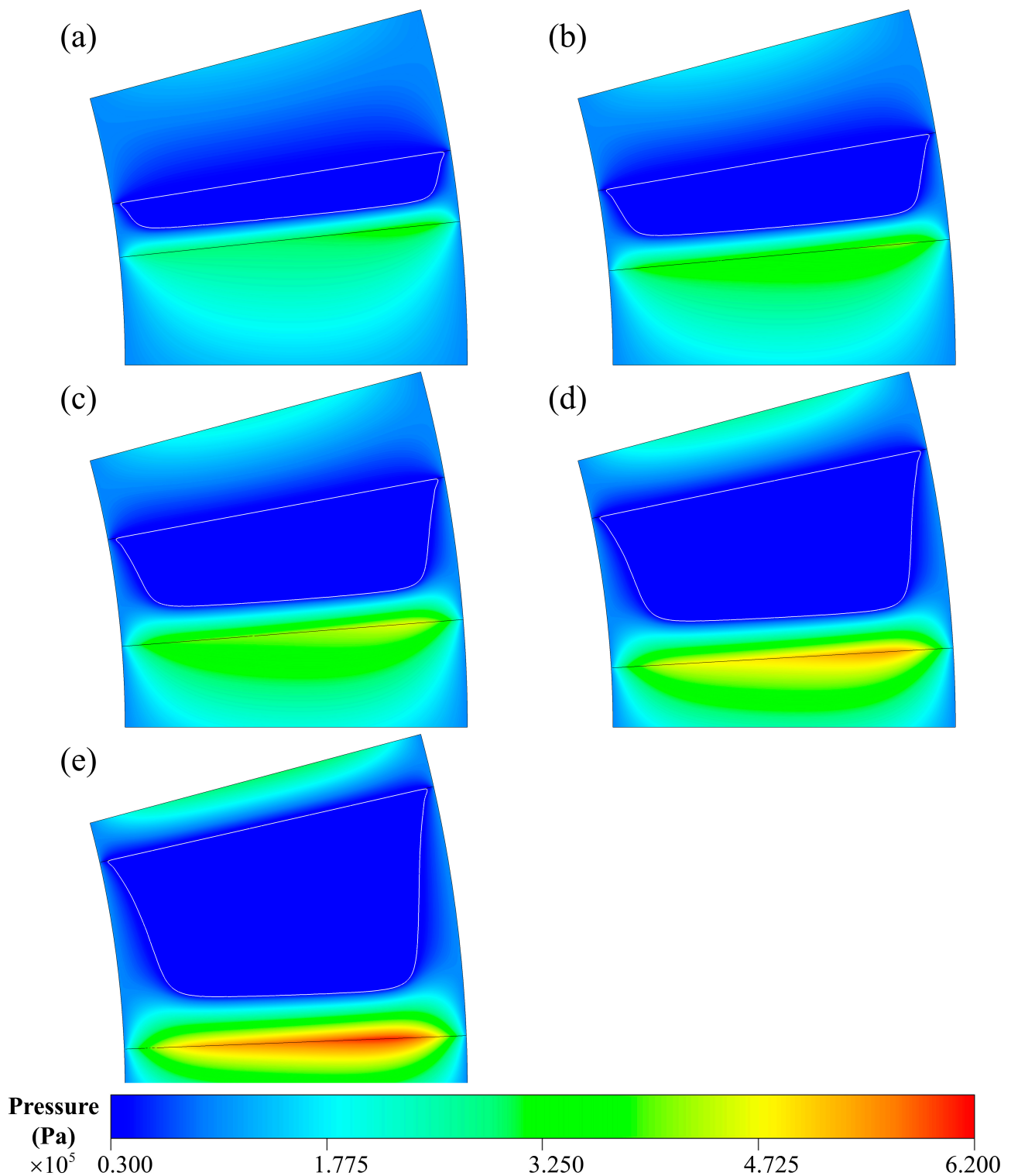


Figure 24. Pressure distribution on the upper ring surface. (a) $AR_g = 0.2$; (b) $AR_g = 0.3$; (c) $AR_g = 0.4$; (d) $AR_g = 0.56$; (e) $AR_g = 0.7$.

As presented in Figure 25, the cavitating area ratio initially increases with the texture area ratio and peaks at 0.56 before gradually decreasing. Similarly, the LCC initially increases and then decreases, reaching its maximum when the texture area is 0.56. Due to the increase in cavitation area shown in Figure 24, the viscosity of the cavitation area is smaller than the oil, so the shear stress and frictional force keep going down. Therefore, the

frictional coefficient first decreases sharply and then slowly. The LCC is largest, and the frictional coefficient is relatively small when the texture area ratio is 0.56.

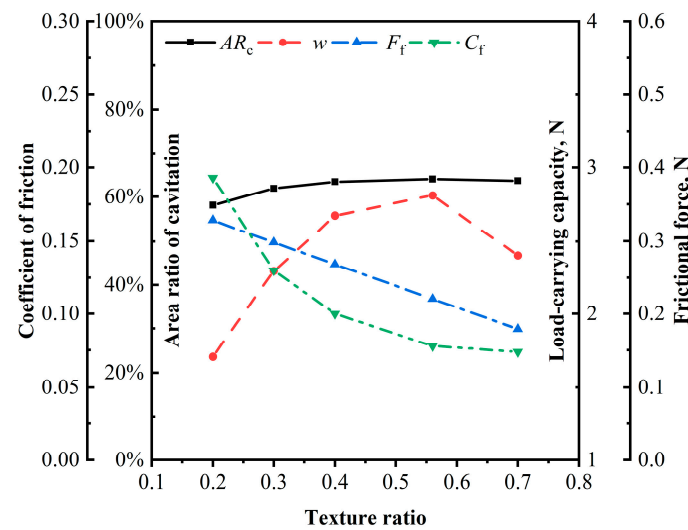


Figure 25. Cavitating area ratio AR_c , LCC w , frictional force F_f , and frictional coefficient C_f at different texture ratios.

As revealed by the numerical simulation, due to the presence of textures, cavitation and vortices occur in the textured region, the low-pressure region and the high-pressure region are formed in the upstream diverging wedge and downstream converging wedge, respectively. The pressure at the inner and outer radii is equal to atmospheric pressure. Thus, the lubricating oil is pushed out and sucked into the textured region in the radial direction, which indicates that surface texture has an apparent side flow effect. The appropriate areas of the vortices in the upstream and downstream facilitate the lubricating oil to flow into and out of the textured zone. Thus, the LCC is improved. However, the occurrence of vortices depends on the appropriate surface texture parameters and operating conditions. Cavitation can prevent the local pressure from dropping below the cavitating pressure and keep the cavitation region an isobaric area of cavitating pressure, which is beneficial to the LCC. However, if the cavitating area is too large, it will compress the peak pressure and area of high pressure, adversely affecting the LCC. Consequently, the coupling effect of vortex and cavitation significantly influences the LCC. Cavitation occurs at the upstream divergent wedge, resulting in a lower viscosity of the air–oil two-phase mixture within the cavitation zone than that of the lubricating oil. As a result, the shear stress and frictional force are diminished.

5. Summary and Conclusions

The three-dimensional CFD model was established to explore the internal flow behavior of straight-groove texture in the thrust bearing, which may further help understand the mechanism of groove texture on tribological properties. The influence of the Reynolds number, depth ratio, and groove texture area ratio on LCC, frictional force, and frictional coefficient C_f was analyzed. The conclusions are as follows:

- (1) The presence of noticeable distortion in the radial streamline indicates the occurrence of side flow within the straight-groove texture.
- (2) The hydrodynamic effect increases with the Re_o , so the LCC increases, accompanied by the frictional force, leading to an increase in the frictional coefficient. The straight-groove texture has an optimal depth ratio and area ratio, maximizing LCC while minimizing the frictional coefficient.
- (3) The LCC is affected by the coupling effect of the vortex and cavitation. The vortices at the upstream and downstream of the texture can facilitate the lubricating oil flow

into and out of the groove-textured region. However, the vortices also consume the kinetic energy of lubricating oil, thereby weakening the LCC. When the positive and negative effects of the vortices reach a certain balance, the tribological properties of the thrust bearing with straight-groove textures will be improved. The cavitation zone contains oil and air phases, resulting in the viscosity of the cavitation zone being lower than that of the oil. Therefore, the shear stress and frictional force in the cavitation area are reduced.

- (4) The location of the circumferential cavitation region in the textured zone can be determined by the boundary where the circumferential velocity is equal to 0 or the extremum points, and the extremum points of the radial velocity can determine the radial location of the cavitating region.

Author Contributions: Conceptualization: Y.H. and Y.L.; methodology: Y.L. and Z.Z.; formal analysis and investigation: Y.H. and Y.L.; writing—original draft preparation: Y.L.; writing—review and editing: Y.L., Y.H. and J.L.; supervision: Y.H. All authors have read and agreed to the published version of the manuscript.

Funding: This research was funded by the National Key Basic Research Program of China (973 Program) (No. 2014CB046404).

Data Availability Statement: The data generated in this research will be available from the corresponding author upon reasonable request.

Conflicts of Interest: The authors declare no conflict of interest.

Nomenclature

| | |
|-----------------------|---|
| AR_c | Area ratio of cavitation |
| AR_g | Area ratio of the groove texture |
| C_f | Frictional coefficient |
| d_g | Texture depth (μm) |
| F_f | Frictional force (N) |
| h_0 | Lubricating film thickness (μm) |
| n_r | Rotating speed of the upper surface (rpm) |
| p | Local film pressure (Pa) |
| p_0 | Ambient pressure (Pa) |
| p_c | Cavitation pressure (Pa) |
| p_{gas} | Pressure of the gas (Pa) |
| r, θ, z | Cylindrical coordinates |
| r_i | Inner radius of the computational domain (mm) |
| r_o | Outer radius of the computational domain (mm) |
| R_c | Source term related to the collapse of gas |
| Re_o | Reynolds number |
| R_f | Source term related to the formation of gas |
| S_c | Cavitating area (mm^2) |
| S_t | Grooved texture area (mm^2) |
| v_c | Circumferential velocity (m/s) |
| $\vec{v}_{dr,k}$ | Drift velocity vector for phase k (m/s) |
| \vec{v}_k | Velocity vector of phase k (m/s) |
| \vec{v}_m | Mass-averaged velocity vector (m/s) |
| v_r | Radial velocity (m/s) |
| w | Load-carrying capacity (N) |
| α_{air} | Air volume fraction |
| α_k | Volume fraction of phase k |
| α_{oil} | Volume fraction of oil |
| η_{air} | Dynamic viscosity of the air (Pa·s) |

| | |
|-----------------|---|
| η_m | Dynamic viscosity of the mixture (Pa·s) |
| η_{oil} | Dynamic viscosity of the oil (Pa·s) |
| θ_0 | Angle of the computational domain (°) |
| θ_g | Groove angle (°) |
| λ_d | Depth ratio of texture |
| ω | Angular velocity (rad/s) |
| ρ_{air} | Air density (kg/m ³) |
| ρ_k | Density of phase k (kg/m ³) |
| ρ_m | Mixture density of air and oil (kg/m ³) |
| ρ_{oil} | Oil density (kg/m ³) |
| \mathcal{R}_B | Radius of the bubble (m) |

References

- Hamilton, D.B.; Walowit, J.A.; Allen, C.M. A theory of lubrication by micro-irregularities. *J. Basic Eng.* **1966**, *088*, 177–185. [\[CrossRef\]](#)
- Etsion, I.; Burstein, L. A Model for Mechanical Seals with Regular Microsurface Structure. *Tribol. Trans.* **1996**, *39*, 677–683. [\[CrossRef\]](#)
- Liu, F.; Li, Y.; Yu, B.; Hao, M.; Sun, X.; Li, Z.; Xu, L. Experimental Research on Sealing Performance of Liquid Film Seal with Herringbone-grooved Composite Textures. *Tribol. Int.* **2022**, *178*, 108005.
- Li, Y.; Brunetière, N.; Hao, M.; Li, T.; Liu, F. Experimental study on transient frictional features of herringbone-grooved mechanical face seals in start-up and stop stages. *Tribol. Int.* **2022**, *175*, 107790. [\[CrossRef\]](#)
- Gu, C.; Meng, X.; Xie, Y.; Li, P. A study on the tribological behavior of surface texturing on the nonflat piston ring under mixed lubrication. *Proc. Inst. Mech. Eng. Part J J. Eng. Tribol.* **2015**, *230*, 452–471. [\[CrossRef\]](#)
- Guo, Z.; Yuan, C.; Liu, P.; Peng, Z.; Yan, X. Study on Influence of Cylinder Liner Surface Texture on Lubrication Performance for Cylinder Liner–Piston Ring Components. *Tribol. Lett.* **2013**, *51*, 9–23. [\[CrossRef\]](#)
- Ma, X.; Wang, Q.J.; Lu, X.; Mehta, V.S. Piston surface design to improve the lubrication performance of a swash plate pump. *Tribol. Int.* **2019**, *132*, 275–285. [\[CrossRef\]](#)
- Chen, L.; Shang, L.; Liu, Z.; Mukherjee, S.; Cai, Y.; Wang, B. Effects of chevron micro-textures on tribological and lubricating performance of cylinder block/valve plate interface in axial piston pumps. *J. Tribol.* **2022**, *145*, 032201. [\[CrossRef\]](#)
- Tang, L.; Liu, Y. Influence of surface micro-texture on the tribological properties of heavy-duty gears. *J. Tsinghua Univ. Sci. Technol.* **2010**, *50*, 1009–1012, 1017.
- Wang, X.; Kato, K.; Adachi, K.; Aizawa, K. Loads carrying capacity map for the surface texture design of SiC thrust bearing sliding in water. *Tribol. Int.* **2003**, *36*, 189–197. [\[CrossRef\]](#)
- Li, Y.; Sun, D.; He, Y.; Luo, J. Coupled Optimization of Groove Texture for Parallel Ring–Ring Friction Pairs: Theory and Experiments. *Tribol. Lett.* **2022**, *70*, 53. [\[CrossRef\]](#)
- Arghir, M.; Roucou, N.; Helene, M.; Frene, J. Theoretical Analysis of the Incompressible Laminar Flow in a Macro-Roughness Cell. *J. Tribol.* **2003**, *125*, 309–318. [\[CrossRef\]](#)
- Sahlin, F.; Glavatskih, S.B.; Almqvist Tr Larsson, R. Two-Dimensional CFD-Analysis of Micro-Patterned Surfaces in Hydrodynamic Lubrication. *J. Tribol.* **2005**, *127*, 96–102. [\[CrossRef\]](#)
- Cupillard, S.; Glavatskih, S.; Cervantes, M.J. Inertia effects in textured hydrodynamic contacts. *Proc. Inst. Mech. Eng. Part J J. Eng. Tribol.* **2010**, *224*, 751–756. [\[CrossRef\]](#)
- Fowell, M.; Olver, A.V.; Gosman, A.D.; Spikes, H.A.; Pegg, I. Entrainment and Inlet Suction: Two Mechanisms of Hydrodynamic Lubrication in Textured Bearings. *J. Tribol.* **2006**, *129*, 336–347. [\[CrossRef\]](#)
- Olver, A.V.; Fowell, M.T.; Spikes, H.A.; Pegg, I.G. ‘Inlet suction’, a load support mechanism in non-convergent, pocketed, hydrodynamic bearings. *Proc. Inst. Mech. Eng. Part J J. Eng. Tribol.* **2006**, *220*, 105–108. [\[CrossRef\]](#)
- Ibatan, T.; Uddin, M.S.; Chowdhury, M.A.K. Recent development on surface texturing in enhancing tribological performance of bearing sliders. *Surf. Coat. Technol.* **2015**, *272*, 102–120. [\[CrossRef\]](#)
- Sahlin, F.; Glavatskih, S.B.; Almqvist Tr Larsson, R. 2D CFD-Analysis of Micro-Patterned Surfaces in Hydrodynamic Lubrication. In Proceedings of the ASME/STLE 2004 International Joint Tribology Conference, Long Beach, CA, USA, 24–27 October 2004; pp. 1657–1665.
- de Kraker, A.; van Ostayen, R.A.J.; van Beek, A.; Rixen, D.J. A Multiscale Method Modeling Surface Texture Effects. *J. Tribol.* **2006**, *129*, 221–230. [\[CrossRef\]](#)
- Dobrica, M.B.; Fillon, M. About the validity of Reynolds equation and inertia effects in textured sliders of infinite width. *Proc. Inst. Mech. Eng. Part J J. Eng. Tribol.* **2009**, *223*, 69–78. [\[CrossRef\]](#)
- Li, J.; Chen, H. Evaluation on Applicability of Reynolds Equation for Squared Transverse Roughness Compared to CFD. *J. Tribol.* **2007**, *129*, 963–967. [\[CrossRef\]](#)
- Dowson, D. Cavitation in lubricating films supporting small loads. *Proc. Conf. Lubr. Wear* **1957**, *93*, 99.
- Zhang, J.; Meng, Y. Direct Observation of Cavitation Phenomenon and Hydrodynamic Lubrication Analysis of Textured Surfaces. *Tribol. Lett.* **2012**, *46*, 147–158. [\[CrossRef\]](#)

24. Li, Q.; Zheng, S.; Liu, S. Influence of cavitation pressure on performance of sliding bearings. *Bearing* **2008**, *12*, 1–4.
25. Shi, X.; Ni, T. Effects of groove textures on fully lubricated sliding with cavitation. *Tribol. Int.* **2011**, *44*, 2022–2028. [[CrossRef](#)]
26. Xie, Z.; Zhang, Y.; Zhou, J.; Zhu, W. Theoretical and experimental research on the micro interface lubrication regime of water lubricated bearing. *Mech. Syst. Signal Process.* **2021**, *151*, 107422. [[CrossRef](#)]
27. Caramia, G.; Carbone, G.; De Palma, P. Hydrodynamic lubrication of micro-textured surfaces: Two dimensional CFD-analysis. *Tribol. Int.* **2015**, *88*, 162–169. [[CrossRef](#)]
28. Shen, Z.; Wang, F.; Chen, Z.; Ruan, X.; Zeng, H.; Wang, J.; An, Y.; Fan, X. Numerical simulation of lubrication performance on chevron textured surface under hydrodynamic lubrication. *Tribol. Int.* **2021**, *154*, 106704. [[CrossRef](#)]
29. Wang, W.; He, Y.; Li, Y.; Wei, B.; Hu, Y.; Luo, J. Investigation on inner flow field characteristics of groove textures in fully lubricated thrust bearings. *Ind. Lubr. Tribol.* **2018**, *70*, 754–763. [[CrossRef](#)]
30. Li, K.; Dalei, J.; Hu, J.; Ding, X.; Yao, Z. Numerical investigation of the tribological performance of micro-dimple textured surfaces under hydrodynamic lubrication. *Beilstein J. Nanotechnol.* **2017**, *8*, 2324–2338. [[CrossRef](#)]
31. Yu, R.; Li, P.; Chen, W. Study of grease lubricated journal bearing with partial surface texture. *Ind. Lubr. Tribol.* **2016**, *68*, 149–157. [[CrossRef](#)]
32. Wei, S.; Kligerman, Y.; Goltsberg, R.; Etsion, I. Variation of Lubricant Distribution Across the Radial Direction in a Journal Bearing. *J. Tribol.* **2021**, *144*, 061803. [[CrossRef](#)]
33. Ansys, I. *ANSYS Fluent Theory Guide*; Ansys, Inc.: Canonsburg, PA, USA, 2021.
34. Song, Z.; Guo, F.; Liu, Y.; Hu, S.; Liu, X.; Wang, Y. Investigation of slip/no-slip surface for two-dimensional large tilting pad thrust bearing. *Ind. Lubr. Tribol.* **2017**, *69*, 995–1004. [[CrossRef](#)]
35. Yang, T.; Cai, J.; Wang, L.; Tang, D.; Chen, S.; Wang, J. Numerical Analysis of Turbulence Effect for Coupled Journal-Thrust Water-Lubricated Bearing with Micro Grooves. *J. Tribol.* **2023**, *145*, 084101. [[CrossRef](#)]
36. Jiang, S.; Ji, H.; Wang, T.; Feng, D.; Li, Q. Enhanced understanding of leakage in mechanical seals with elliptical dimples based on CFD simulation. *Ind. Lubr. Tribol.* **2020**, *72*, 24–30. [[CrossRef](#)]

Disclaimer/Publisher’s Note: The statements, opinions and data contained in all publications are solely those of the individual author(s) and contributor(s) and not of MDPI and/or the editor(s). MDPI and/or the editor(s) disclaim responsibility for any injury to people or property resulting from any ideas, methods, instructions or products referred to in the content.